PAPER

CORSICA modelling of ITER hybrid operation scenarios[b]

IOP Publishing | International Atomic Energy Agency Nuclear Fusion

Nucl. Fusion **56** (2016) 126002 (19pp) doi:10.1088/0029-5515/56/12/126002

CORSICA modelling of ITER hybrid operation scenarios[b]

S.H. Kim[1], R.H. Bulmer[2], D.J. Campbell[1], T.A. Casper[1,a], L.L. LoDestro[2], W.H. Meyer[2], L.D. Pearlstein[2] and J.A. Snipes[1]

[1] ITER Organization, Route de Vinon-sur-Verdon, CS 90 046, 13067 St. Paul Lez Durance Cedex, France
[2] Lawrence Livermore National Laboratory, PO Box 808, Livermore, CA 945550, USA

E-mail: sunhee.kim@iter.org

Received 23 March 2016, revised 10 June 2016
Accepted for publication 13 July 2016
Published 31 August 2016

Abstract

The hybrid operating mode observed in several tokamaks is characterized by further enhancement over the high plasma confinement (*H*-mode) associated with reduced magneto-hydro-dynamic (MHD) instabilities linked to a stationary flat safety factor (q) profile in the core region. The proposed ITER hybrid operation is currently aiming at operating for a long burn duration (>1000 s) with a moderate fusion power multiplication factor, Q, of at least 5. This paper presents candidate ITER hybrid operation scenarios developed using a free-boundary transport modelling code, CORSICA, taking all relevant physics and engineering constraints into account. The ITER hybrid operation scenarios have been developed by tailoring the 15 MA baseline ITER inductive *H*-mode scenario. Accessible operation conditions for ITER hybrid operation and achievable range of plasma parameters have been investigated considering uncertainties on the plasma confinement and transport. ITER operation capability for avoiding the poloidal field coil current, field and force limits has been examined by applying different current ramp rates, flat-top plasma currents and densities, and pre-magnetization of the poloidal field coils. Various combinations of heating and current drive (H&CD) schemes have been applied to study several physics issues, such as the plasma current density profile tailoring, enhancement of the plasma energy confinement and fusion power generation. A parameterized edge pedestal model based on EPED1 added to the CORSICA code has been applied to hybrid operation scenarios. Finally, fully self-consistent free-boundary transport simulations have been performed to provide information on the poloidal field coil voltage demands and to study the controllability with the ITER controllers.

Keywords: ITER, CORSICA, hybrid operation scenario

(Some figures may appear in colour only in the online journal)

1. Introduction

ITER[c] will explore advanced tokamak operation regimes, such as the hybrid and steady-state operating modes, to demonstrate the feasibility of fusion energy production at a reactor scale with deuterium and tritium fuels. The hybrid operating mode observed in several tokamaks [1–5] is characterized by further confinement improvement over the conventional high-confinement-mode (*H*-mode) plasma operation. This confinement improvement may be associated with low-level magneto-hydro-dynamic (MHD) instabilities for a stationary flat safety factor (q) profile in the core region, although the physics understanding of the self-regulating mechanism on the safety factor profile ($q > 1.0$) needs to be further investigated [6, 7]. The hybrid operating mode will be of a particular interest in ITER as it will be a step toward a long pulse operation with a high neutron fluence, which is important for demonstrating engineering capabilities for reactor-relevant operation in future reactors. The ITER hybrid operation is currently aiming at operating the plasma for a long burn duration (up to 1000 s)

[a] Now at 1166 Bordeaux St Pleasanton, CA 94566, USA.
[b] Extended from *Proc. 24th Int. Conf. on Fusion Energy (San Diego, 2012)* IT/P1-13.
[c] ITER is a Nuclear Facility INB-174.

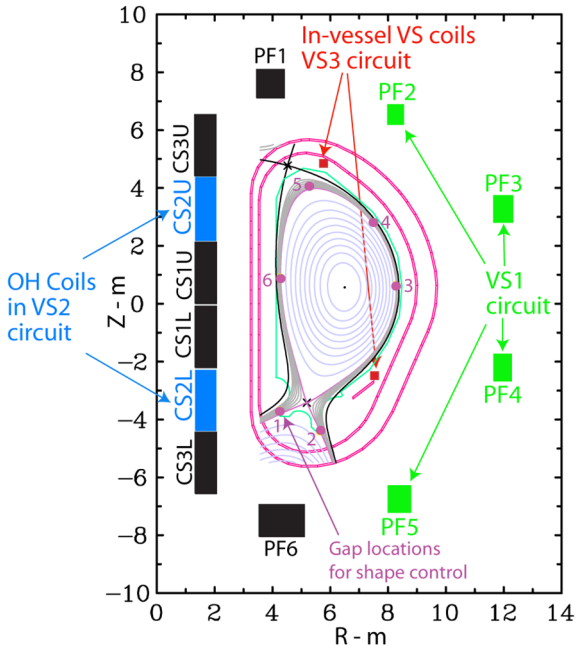

Figure 1. CORSICA model of ITER coil systems and conducting structures. Reprinted with permission from [13]. Copyright 2014 IAEA.

with a moderate fusion power multiplication factor (Q) of at least 5. The key element to hybrid operating mode is to tailor the plasma current density profile, therefore to form a flat q profile (>1) at the beginning of the flat-top phase without triggering sawtooth crashes [8, 9] and to maintain it during the burn phase. However, it is a challenging issue when auxiliary heating and current drive (H&CD) sources are limited in terms of available power and accessibility [10]. In ITER, the hybrid operating mode will be demonstrated at a lower flat-top plasma current of about 11–13 MA with a reduced flat-top density and an increased q_{95} (safety factor at 95% of flux surface) of about 4 [11, 12], compared with the 15 MA baseline inductive H-mode operation [13]. This paper focuses on developing feasible hybrid operation scenarios of ITER, taking both physics and operational aspects into account. Investigating details of the hybrid operating mode and improving physics understanding will be a subject of further study in existing tokamak experiments and also in future ITER experiments.

Development of feasible ITER operation scenarios requires an integrated tokamak discharge simulator, such as CORSICA [13, 14], DINA-CH/CRONOS [9, 15, 16], TSC [17, 18], PTRANSP [19], JINTRAC/CREATE-NL [20, 21], and ETS [22, 23]. The DINA-CH/CRONOS simulator was developed by combining a free-boundary equilibrium evolution code, DINA-CH, and an advanced transport and source modelling code, CRONOS. It uses an explicit code coupling and data exchange scheme, requiring small time-steps to obtain good convergence and self-consistency. The TSC free-boundary evolution code assumes a finite plasma mass for the inertial term in the force balance equation [24], differently with DINA-CH and CREATE-NL which assume the plasma response is governed by massless electro-magnetic interactions. The PTRANSP code, as an extended version of TRANSP with more rigorous predictive capability, is developed for integrated transport modelling of tokamak discharges. The JINTRAC/CREATE-NL simulator is developed by coupling a transport modelling code, JINTRAC, and a free-boundary equilibrium code, CREATE-NL. It may require further improvement in its 'strong' coupling schemes for fully self-consistent discharge modelling with a reasonable computational performance. The European transport solver, ETS, is being developed by the European integrated tokamak modelling (EU-ITM) activity [23] using the Kepler framework environment [25] which is a basis for developing the ITER integrated modelling analysis suite (IMAS) [26]. The CORSICA simulator provides self-consistent evolution of the free-boundary plasma equilibrium and transport using its fully implicit code coupling scheme, as well as high computation performance which is essential for simulating entire operation phases over 1000 s. However, the CORSICA code previously used for the 15 MA ITER baseline inductive H-mode operation [13] had only a few realistic source modules which were not sufficient for studying ITER advanced operation scenarios.

In this work, several realistic source modules for heating and current drive (H&CD), such as the neutral beam (NB) injection, electron and ion cyclotron (EC&IC), and lower hybrid (LH), are either upgraded or newly added to the CORSICA code using the ITER H&CD system configurations. We have then developed several ITER hybrid operation scenarios, including relevant physics and engineering constraints on the poloidal field coils, power supply systems and controllers. Note that the major ITER poloidal field coils are categorized as CS (central solenoid) and PF (non-CS) coils, and VS coils stand for vertical stabilization coils (see figure 1). The ITER hybrid operation scenarios have been studied focusing on achieving several operation goals, such as the fusion power multiplication factor and plasma burn duration. Although feasible ITER operation scenarios for hybrid operating mode have been successfully achieved in this work, those scenarios will be further optimized in the future as physics understanding of the tokamak plasma, plasma operation, and integrated modelling capability are improved.

In section 2, we present a 12.5 MA ITER hybrid operation scenario developed by tailoring the 15 MA ITER inductive H-mode scenario. This scenario is used as a reference case for comparison in this paper. In section 3, we have investigated accessible conditions for ITER hybrid operating mode and achievable range of plasma parameters. Operational capabilities of avoiding ITER poloidal field coil current, field and force limits are examined by applying different operation methods and techniques. Several physics issues, such as plasma current density profile tailoring, enhancement of the plasma energy confinement, and fusion power generation have been investigated by applying various combinations of external H&CD. The flat-top plasma density and density peaking factor have also been varied to examine the changes in operation conditions for ITER hybrid operations. A parameterized edge pedestal model based on EPED1 [27] added to the CORSICA code has been applied to hybrid operation scenarios. Note that these studies in sections 2 and 3 have performed using 'backing-out' mode [28] of the CORSICA

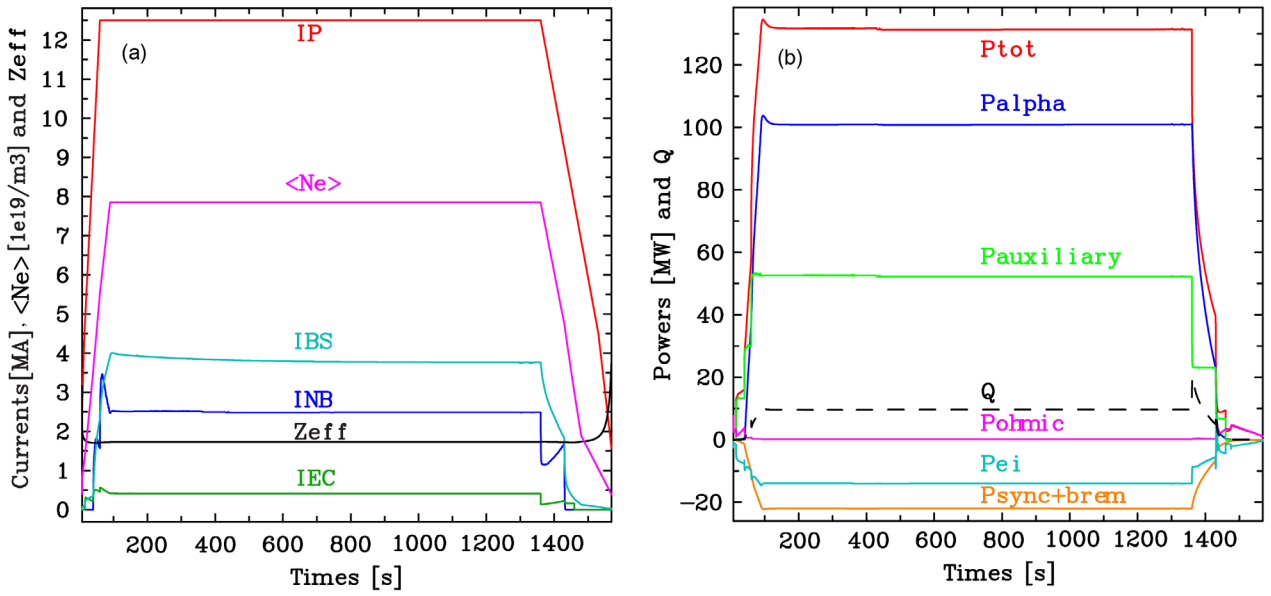

Figure 2. 12.5 MA ITER hybrid operation scenario (reference simulation case). (*a*) Time traces of the plasma current (I_p), driven currents from neutral beam (I_{NB}) and electron cyclotron (I_{EC}) injected power, bootstrap current (I_{BS}), volume averaged electron density ($\langle N_e \rangle$) and effective charge number (Z_{eff}). (*b*) Time traces of the total heating power (P_{tot}), alpha particle self-heating power (P_{alpha}), auxiliary heating power ($P_{auxiliary}$), ohmic heating power (P_{ohmic}), electron–ion equipartition power ($P_{ei} < 0$ for power flow from electrons to ions), synchrotron and bremsstrahlung radiation powers ($P_{sync+brem}$) and fusion power multiplication factor (Q).

code, which performs a free-boundary equilibrium calculation at every time-step to compute the evolution of poloidal field coil currents required for providing the plasma boundary close to prescribed waveforms. This mode of computation provides most of the information required for developing operation scenarios, except the power supply voltage demands computed by controllers and eddy currents flowing in the passive conducting structures. Therefore, a fully self-consistent free-boundary calculation including controllers, power supply and passive conducting structure models is additionally required for 'forward' mode free-boundary control simulation. Details of these computation modes are explained in the reference [13]. In section 4, fully self-consistent free-boundary control simulations have been performed to provide information on the poloidal field coil voltage demands and to study the controllability of the plasma with the existing ITER controllers. A summary and discussion are presented in section 5.

2. Simulating ITER hybrid operation scenarios

Several important quantitative and qualitative aspects in developing the ITER hybrid operation scenarios have been introduced in this paper, by comparing potential candidate scenarios developed with different assumptions. To perform a systematic analysis, one of a number of 12.5 MA hybrid operation scenarios has been selected as a reference scenario, and then it has been compared with its variants. This reference scenario has been developed including the most common modelling and operation assumptions introduced in detail in section 2.1. Note that this reference scenario is not necessarily the representative ITER reference hybrid operation scenario which will be continuously developed taking all the improved physics understanding and relevant operation constraints.

2.1. Modelling assumptions and simulation settings

ITER hybrid operation scenarios have been developed by tailoring the 15 MA ITER inductive *H*-mode scenario [13] and expanding the flat-top burn duration up to $t = 1300$ s as shown in figure 2. The plasma current is ramped up to 12.5 MA in 60 s and an *L-H* confinement mode transition is assumed at about 2/3 of the current ramp-up duration ($tL2H \sim 40$ s). The plasma is assumed to start with a larger bore limited on the inboard wall, and then it is allowed to grow along with the plasma current and experience a shape transition from a limited to a diverted configuration ($t\mathrm{DIV} \sim 15$ s, see figure 3(*a*)). The EC power is switched on after the shape transition to deliver 13.34 MW of power to the plasma, and then one neutral beam injector (16.5 MW) is switched on at $t = 40$ s. It has been assumed that this amount of auxiliary heating triggers an *L-H* confinement mode transition at $t = 40$ s in the reference simulation, although the auxiliary heating power applied of about 30 MW seems to be lower than the *H*-mode threshold power estimated by the Martin's *H*-mode threshold power scaling law [29]. As the validity of this assumption and attainability of the *H*-mode during the current ramp-up can significantly impact the development of feasible hybrid operation scenarios, it has been investigated in detail later in section 3.5. At the start of the flat-top phase ($t\mathrm{SOF} \sim 60$ s), the total NB power is increased to 33 MW by switching on another injector and the total EC power is increased to 20 MW by adding 6.77 MW of additional power. As the plasma temperature and density increase with the additional auxiliary power, the plasma self-heating by fusion-born alpha particles becomes significant. The current flat-top is maintained for about 1300 s of burn duration until the end of the flat-top phase ($t\mathrm{EOF} \sim 1360$ s), and then the plasma current is ramped down for about 210 s. During the ramp-down phase, the plasma shape evolution is designed

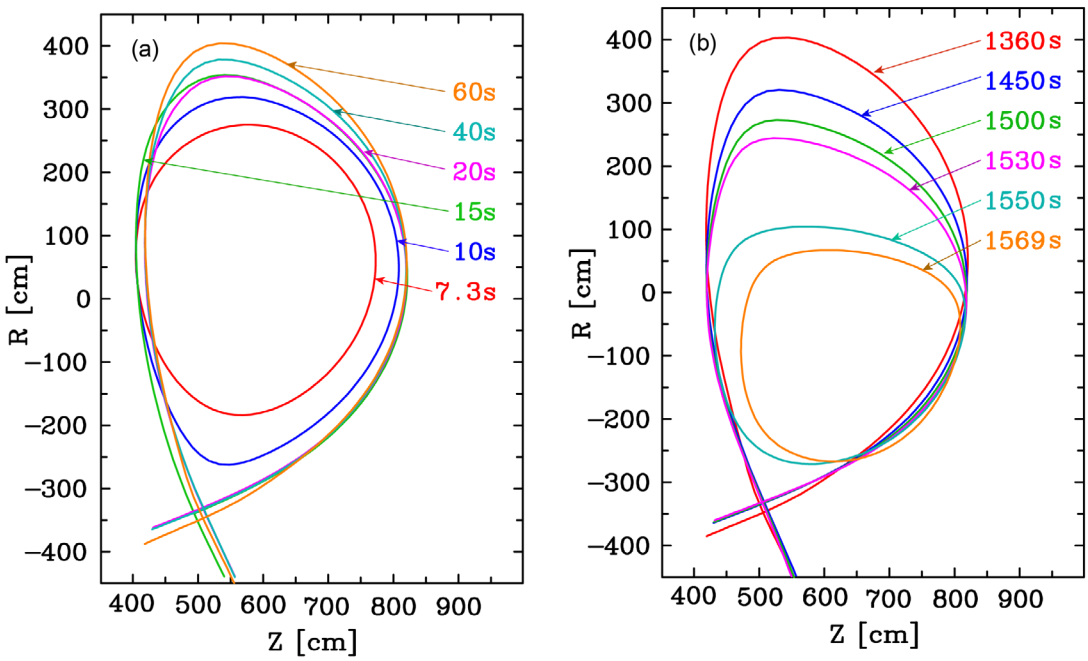

Figure 3. Prescribed plasma shape evolution during the ramp-up (*a*) and ramp-down (*b*) in the reference 12.5 MA ITER hybrid operation simulation (tDIV ~ 15 s, $tL2H$ ~ 40 s, tSOF ~ 60 s, tEOF ~ 1360 s and tH2L ~ 1430 s).

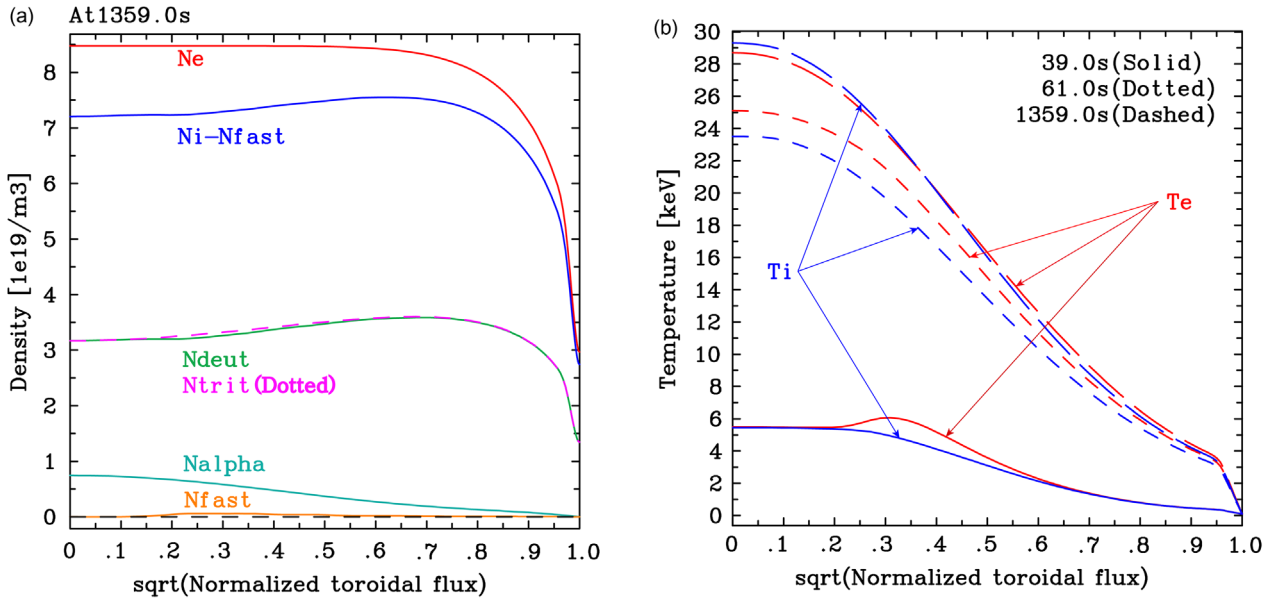

Figure 4. The density profiles (*a*) and electron (T_e) and ion (T_i) temperature profiles (*b*) in the reference 12.5 MA ITER hybrid operation simulation ($tL2H$ ~ 40 s, tSOF ~ 60 s and tEOF ~ 1360 s): densities of electrons (N_e), total ions (N_i), deuterium (N_{deut}), tritium (N_{trit}), alpha particles (N_{alpha}), and neutral beam fast ion (N_{fast}).

to experience a downward shift and the plasma elongation is slowly reduced to mitigate the growth of the vertical instability. The diverted plasma shape configuration is maintained until the plasma current is reduced low enough (see figure 3(*b*)). An *H-L* confinement mode transition is assumed to be at about 1/3 of the current ramp-down duration ($tH2L$ ~ 1430 s). 6.67 MW of EC power has been maintained even after the *H-L* confinement mode transition to allow a smooth transition with a reduced plasma beta drop. The details on the *H-L* confinement transition have not yet been fully investigated in this work due to the uncertainties on dynamic evolution of alpha-particle self-heating power which is sensitive to assumptions used for the density evolution during and after the *H-L* transition.

The central electron density ($n_e(0)$) is linearly increased up to $6.0 \times 10^{19}\,\mathrm{m}^{-3}$ during the current ramp-up phase, while the electron density profile evolution is prescribed to evolve from a parabolic *L*-mode shape to a flat *H*-mode shape (see figure 4(*a*)). Note that the density profile peaking has been investigated in detail later in section 3.3. The central electron density is further increased up to $8.5 \times 10^{19}\,\mathrm{m}^{-3}$ (about

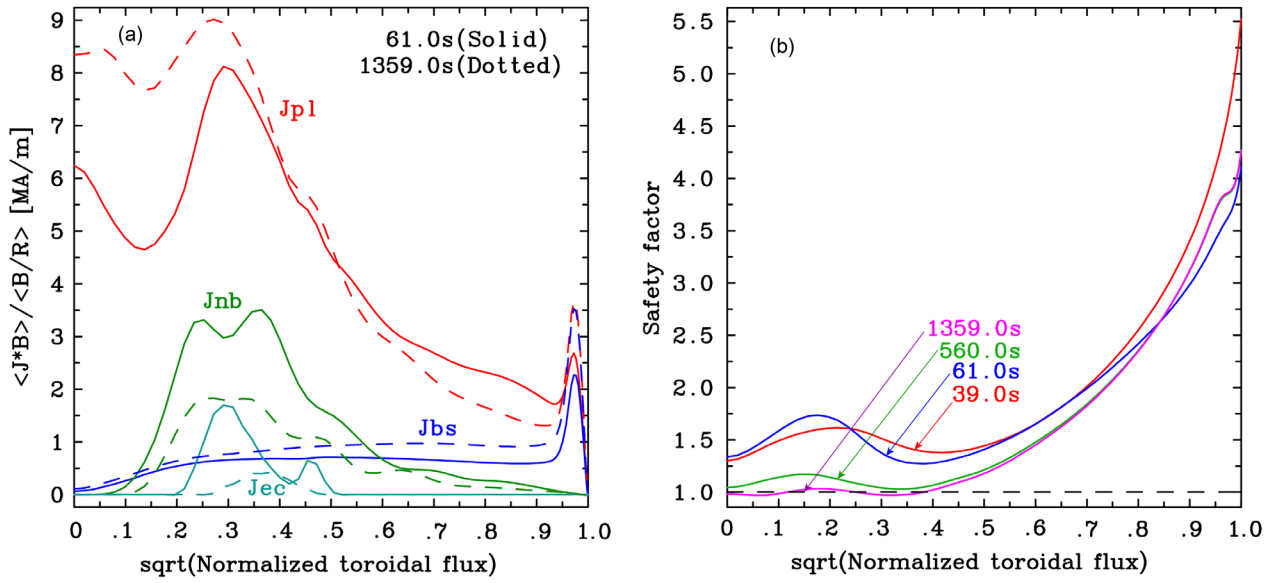

Figure 5. The plasma (J_{pl}), bootstrap (J_{bs}), and NB and EC driven current (J_{ec} and J_{nb}) density profiles (*a*) and safety factor profiles (*b*) in the reference 12.5 MA ITER hybrid operation simulation ($tL2H$ ~ 40 s, tSOF ~ 60 s and tEOF ~ 1360 s).

85% of the Greenwald density limit) for about 30 s after the start of flat-top phase. The electron density at the plasma boundary is assumed to be 35% of the central electron density. The deuterium and tritium fuel ratio is assumed to be 50:50, taking the neutral beam injected deuterium ions into account. Both the deuterium and tritium ion densities become a little hollow for the flat electron density profile due to the quasi-neutrality constraint, as fusion-born alpha particles are produced (see figure 4(*a*)). The alpha particle density profile becomes peaked at the centre. Argon (Ar) and Beryllium (Be) ions are used as main impurity species and their density evolutions are self-consistently calculated with the assumed effective charge number (Z_{eff}), satisfying the quasi-neutrality conditions. The average effective charge number given by adopting Lukash's formulary [30] starts from about 4.0 at the beginning of ramp-up, and then it is reduced as the density increases and maintained around 1.7 during the flat-top phase. The neutral beam fast ions contribution to the deuterium ion density is computed by a neutral beam injection code imbedded in CORSICA, NFREYA [31]. The losses of fast ions and beam driven current are computed from a first orbit model coupled with NFREYA. The heat transport is computed using the Coppi–Tang transport model [32, 33]. The pedestal temperatures are determined by an assumed reduction of the heat conductivities outside $\rho_{tor} = 0.95$, where ρ_{tor} is the square root of the normalized toroidal flux. The heat transport at the pedestal region is assumed to be slightly higher than that used in the 15 MA inductive *H*-mode scenarios [7], to reduce the pedestal top temperatures at around 3–4 keV (see figure 4(*b*)). However, at the core region, the heat transport is slightly reduced to obtain the enhanced core confinement level observed in many hybrid operating modes. Triggering of sawtooth crashes is also modelled by changing the heat conductivities and plasma resistivity inside the inversion radius, when the minimum safety factor, q_{min}, becomes less than 0.97.

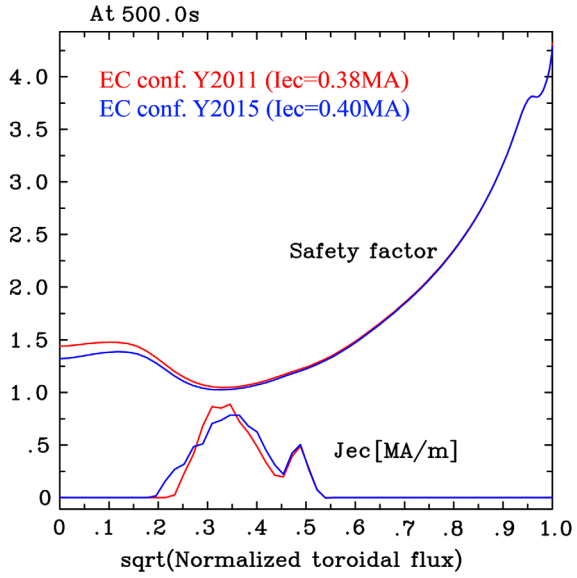

Figure 6. Comparison of the EC driven current and safety factor profiles obtained using the ITER EC configurations in 2011 and 2015 (poloidal mirror steering). The EC driven currents are indicated in the figure for both cases and the density profile peaking factor of 1.3 is applied during the flat-top phase.

Two off-axis neutral beams (poloidal angle = −3.331°) are assumed with the latest design of the ITER neutral beam injection system [34, 35] to deliver up to 33 MW of auxiliary heating power and also to produce a broad plasma current density profile required for a flat q profile at the core (see figure 5). Note that a potential optimization for reducing neutral beam fast ion profile gradients by combining on-axis and off-axis neutral beams is not yet considered in this work. The plasma current density profile is further optimized by using the 170 GHz EC H&CD system consisting of an equatorial launcher (EL) with top, middle and bottom mirrors, and four upper launchers (ULs) with upper and lower steering mirrors [36].

Table 1. Plasma parameters achieved with various H&CD systems at EOF ($t = 1359$ s).

At EOF ($t = 1359$ s)	NB33/ EC20 (ref.)	NB33/EC40	NB33/ EC20/IC20	NB33/ EC20/LH20	NB33/EC20/ LH20/IC20	EC40/LH20	EC40/IC20
W_{th} (MJ)	361.3	389.0	391.2	390.0	416.3	373.4	379.7
H_{98}	1.261	1.278	1.271	1.271	1.282	1.275	1.283
β_N	2.516	2.709	2.722	2.712	2.887	2.500	2.545
$l_i(3)$	0.745	0.723	0.715	0.622	0.592	0.655	0.722
$q(0)$	0.982	1.035	0.958	1.219	1.317	0.972	0.972
q_{min}	0.971	0.987	0.969	1.087	1.210	0.970	0.971
I_{BS} (MA)	3.76	4.09	4.10	4.30	4.65	4.06	3.95
I_{NB} (MA)	2.49	2.65	2.62	2.68	2.72	—	—
I_{EC}/I_{LH} (MA)	0.41/—	0.82/—	0.41/—	0.41/0.90	0.41/0.89	0.82/0.90	0.82/—
P_α (MW)	100.9	110.7	115.7	111.6	124.6	102.5	108.4
P_{loss} (MW)	131.4	159.1	164.7	160.1	191.0	139.3	145.8
P_{aux} (MW)	52.30	72.64	72.65	72.64	92.31	59.99	59.99
Q	9.64	7.63	7.97	7.69	6.76	8.53	8.93
$T_e(0)$ (keV)	28.71	31.61	31.26	31.32	33.27	29.85	30.31
$T_i(0)$ (keV)	29.31	30.96	31.98	30.68	33.03	29.40	30.38
$T_{e,ped}$ (keV)	3.56	3.84	3.82	3.94	4.12	3.77	3.70
Flux (Wb)	−90.22	−82.91	−84.74	−74.79	−70.88	−87.79	−96.35

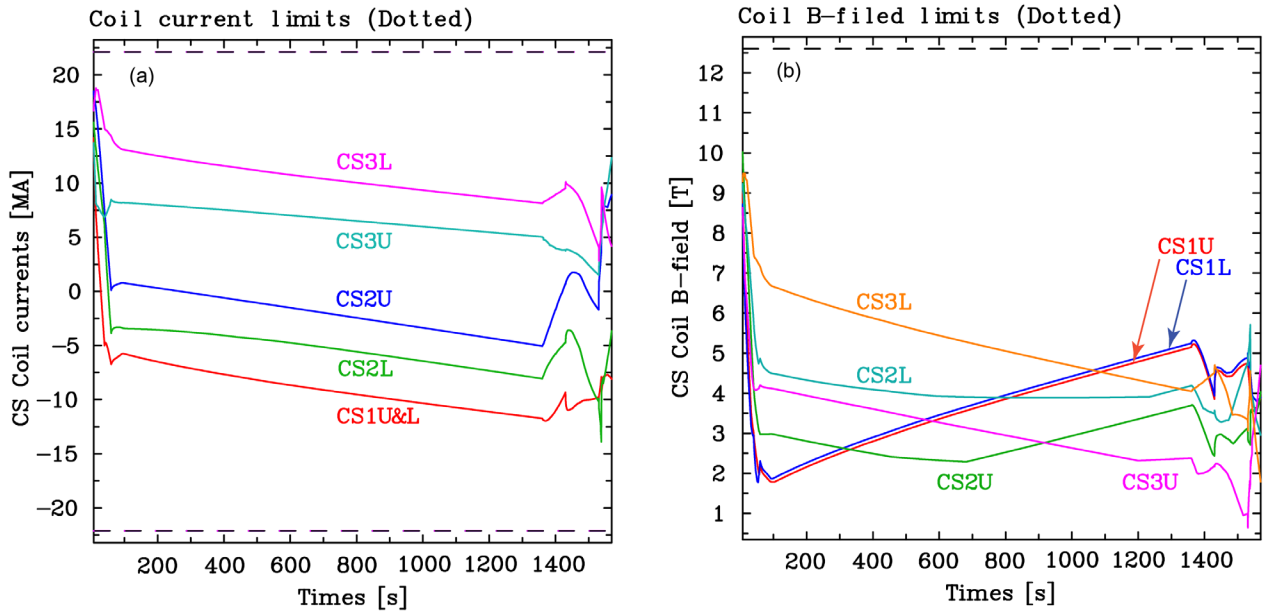

Figure 7. Time traces of the CS coil current (*a*) and applied *B*-field (*b*) coil currents in the reference 12.5 MA ITER hybrid operation simulation. Dotted lines represent the coil current limits. The coil locations are shown in figure 1.

During the flat-top phase, the EL is assumed to deliver about 13.34 MW to provide driven currents at about $\rho_{tor} = 0.2$–0.4 in the co-current direction. The four ULs are assumed to deliver about 6.67 MW aiming at providing far-off-axis current at about $\rho_{tor} = 0.4$–0.6, however at reduced CD efficiency. The angles are determined to better tailor the total plasma current density profile (see figure 5(*a*)), rather than simply to maximize the EC driven current at off-axis location. The electron heat deposition and EC driven current are computed using a ray-tracing code, TORAY-GA [37]. The ITER EC system configuration has been recently updated to provide higher off-axis driven current and improved accessibility [38–40]. The direction of the EL mirror steering has been changed from the toroidal to poloidal and the EL top mirrors are chosen for counter-current drive. In the previous ITER EC configuration ('Y2011'), the EL middle mirrors were chosen for counter-current drive. As the update of ITER EC system configuration ('Y2015') has been decided in the course of this work, the previous ITER EC system configuration has been used for the most of ITER hybrid scenarios presented in this work. To investigate the validity of these simulations, a few simulations have been additionally performed using the updated ITER EC system configuration and the results are compared in figure 6. The variation in the plasma parameter evolution and overall performance were very small as the increase in the EC driven current (0.02 MA) with the updated ITER EC system configuration was only about 0.16% of the total plasma current. The largest difference was observed in the evolution of the safety

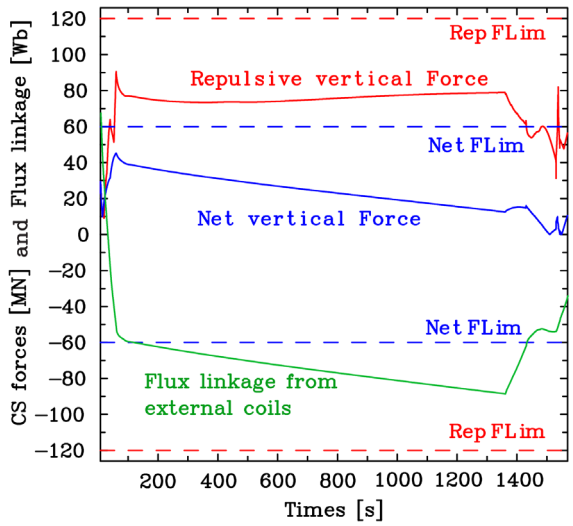

Figure 8. Time traces of the applied forces on CS coils and flux linkage from external poloidal field coils in the reference 12.5 MA ITER hybrid operation simulation. Dotted lines represent the coil force limits.

factor profile inside the EC deposition location. The EC driven current profile obtained using the updated EC configuration is slightly broader and the safety factor inside the EC deposition location became flatter, however without significant change in $q_{\min}$. This change in the safety factor profile appears to be favourable for hybrid operation which requires low magnetic shear at the core region. The difference in the safety factor profile became negligible with the relaxation of the current profile at a later time in the flat-top phase. Note that the ITER EC system configuration may be subject to further improvement as its design is not yet completed.

2.2. The reference ITER hybrid operation scenario for comparison studies

A 12.5 MA hybrid operation scenario has been selected as the reference scenario for comparison with its variants. In this reference scenario, the alpha particle self-heating power was about 100 MW and the fusion power multiplication factor, Q, was above 9.0 during the plasma burn (see figure 2(*b*)). Higher Q (>5) value was obtained at a relatively low auxiliary heating power of 53 MW, assuming the plasma confinement enhancement in hybrid operating modes observed at several devices. Note that the heat diffusivities computed by the Coppi–Tang transport model is adjusted once for the reference hybrid scenario to increase the confinement enhancement factor with respect to H-mode confinement (H_{98}) to 1.2–1.3. Then, the same adjustment has been used for all other variants of this reference scenario. The confinement enhancement factor can be slightly increased along with the total auxiliary heating power (see table 1) and plasma density (see section 3.3) due to the heat diffusivity dependence on the total heating power and plasma density [32, 33], which is the physics feature of the Coppi–Tang transport model.

The safety factor profile, which was initially slightly reversed, became flat in the core region ($\rho_{\text{tor}} < 0.4$–0.5) late in the discharge as shown in figure 5(*b*). The safety factor profile was maintained above 1.0 for a significant fraction (until $t \sim 560$ s) of the current flat-top phase. Even at later time, the flat core q profile was maintained around 1.0 with sawteeth triggered when $q_{\min} < 0.97$. Note that the detailed investigation of the self-regulating mechanism for maintaining the safety factor over 1.0 by proper application of auxiliary heating and current driven in hybrid operating modes is not a main research subject of this paper. Note also that modelling of sawtooth dynamics was not of particular interest in this study, as the safety factor can be maintained over 1.0 in hybrid operating modes, without triggering sawteeth. The plasma current density profile (see figure 5(*a*)) became slightly peaked at the EOF as the non-inductively driven current fraction was not 100% during the flat-top. The edge bootstrap current density was lower at the SOF ($t \sim 60$ s) than that at the EOF ($t \sim 1360$ s), due to the lower plasma density (the density ramp-up was finished at about $t \sim 90$ s). The neutral beam and EC driven currents were higher at lower plasma density.

The internal inductance, $l_{\text{i}}(3)$, was 0.70–0.75 which appears to be beneficial for stabilization of the vertical instability. The normalized beta of about 2.5, the plasma stored energy of about 360 MJ and the volume averaged electron density of about $7.9 \times 10^{19}\,\text{m}^{-3}$ were obtained at the EOF. The bootstrap current was about 3.8 MA and the neutral beam and EC driven currents were about 2.5 MA and 0.4 MA, respectively. A non-inductive current fraction of about 54% was achieved, but it was not enough to maintain the central q value >1.0 until the EOF. The edge safety factor, q_{95}, was 3.7–3.8 during the flat-top phase ($I_{\text{p}}/B_{\text{T}} = 12.5$ MA/5.3 T). Several plasma parameters important for comparison with its variants (see section 3) are summarized in table 1.

The CS coils were well within their coil current, field and force limits specified in the document summarizing the ITER CS and PF coil data and requirements [41] (see figures 7 and 8). The poloidal flux consumption (see figure 8) was large during the current ramp-up whereas it became much smaller during the current flat-top. The poloidal flux was recovered during the current ramp-down. The CS coil power supplies could provide additional poloidal flux for a longer flat-top duration, as the available volt-seconds were not fully consumed at the EOF ($t \sim 1360$ s). Note that the maximum possible duration of the flat-top phase was not investigated in this study, as it appears to be a non-critical issue for ITER hybrid operation. The CS1U and CS1L coils, which are close to the plasma centre (see figure 1), were most demanding in terms of the volt-second consumption during the ramp-up phase and in terms of coil current evolution during the flat-top phase (see figure 7(*a*)). The applied B-fields to the CS coils were quickly reduced during the current ramp-up and stayed away from the B-field limits during the flat-top phase (see figure 7(*b*)). Both net and repulsive vertical forces applied to the CS coils [41] were increased during the current ramp-up but stayed below the limits (see figure 8).

The PF coils were also investigated against their coil current, field and force limits [41] and several potential violations have been identified. Firstly, it appears that the PF6 coil briefly violated its current limit at the end of the current

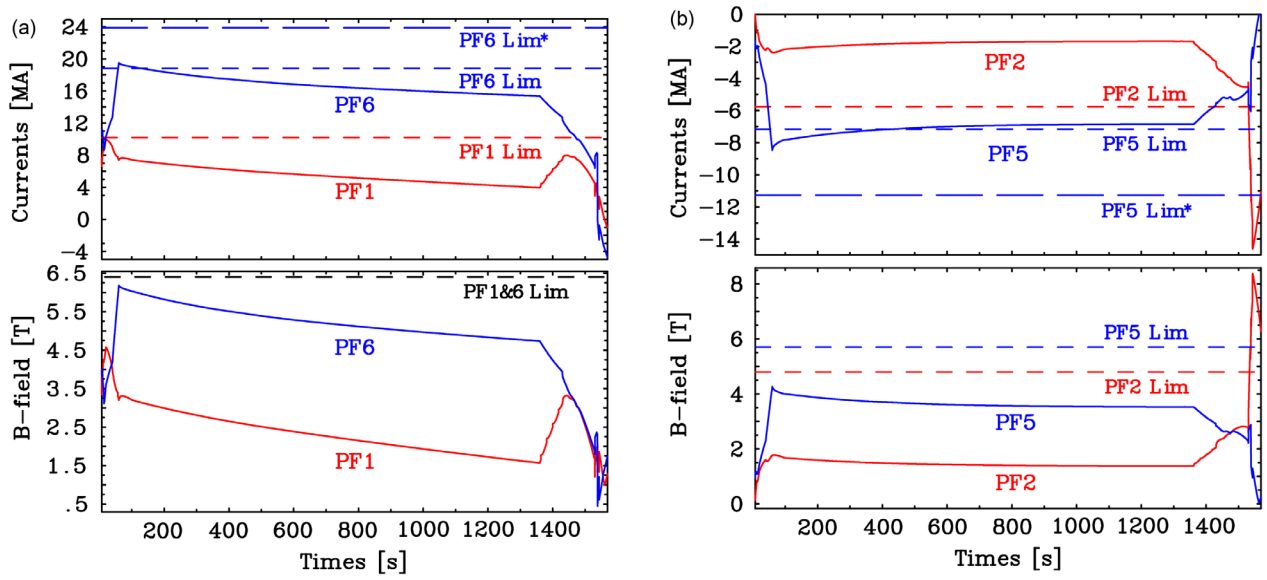

Figure 9. Time traces of the PF1&6 (*a*) and PF2&5 (*b*) coil currents (top) and applied *B*-fields (bottom) in the reference 12.5 MA ITER hybrid operation simulation. Dotted lines represent the coil current limits.

ramp-up phase (see figure 9(*a*)). However, this PF6 coil current limit (~18.8 MA) is specified when the maximum *B*-field applied to the PF6 coil (B_{max}) is 6.5 T. The PF6 coil current limit can be increased up to about 22 MA, if the applied maximum *B*-field is lower than 6.4 T as it is the case shown in figure 9(*a*). Therefore, the PF6 coil current was within its limit in the reference simulation. As the PF6 coil current will be critical for operating the plasma in a diverted configuration, an additional technique, 0.4 K sub-cooling of the coil, has been considered to further increase the PF6 coil limit up to about 23–24 MA with $B_{max} = 6.8$ T [41]. This highest PF6 current limit is additionally shown as 'PF6 Lim∗' in figure 9(*a*) and the PF6 coil current was well below this limit. However, the PF6 coil current violation may happen if the plasma evolution significantly deviates from the one obtained in this simulation. Therefore it is important to develop alternative techniques useful for avoiding such violations and for allowing more operational margins. Several candidate techniques have been attempted in this work as will be shown in section 3.1.

Secondly, the PF2 coil violated its coil current, force and field limits during the ramp-down phase (see figure 9(*b*)). The imbalance current in the VS1 position control system (see figure 1), which is a combination of PF2–PF5 coil currents, also violated its limit during the ramp-down phase. It appears that these violations have happened by rapidly shifting the plasma downward during the ramp-down phase (see figure 3(*b*)) and can be avoided by modifying the ramp-down shape evolution. Although such avoidance has been attempted in section 3.1 as a demonstration of a potential approach, a more complete optimization would be required to consider many other issues associated with the vertical instability, heat load to the plasma facing components, and disruption avoidance. Note that the development of the ITER pulse termination strategy will be a subject of future scenario studies.

Thirdly, it appears that the PF5 coil current violated its limit (~7 MA) specified with $B_{max} = 6.0$ T. However, this limit can be increased up to about 11 MA (indicated as 'PF5 Lim∗'), if the applied maximum *B*-field is lower than 5.7 T. As this is the case in this reference scenario (see figure 9(*b*)), the PF5 coil current was well within its limit. Lastly, the PF1 coil current was very close to its limit at the SOF, although it did not violate its limit in the reference scenario. Therefore the techniques investigated for avoiding CS1 and PF6 coil current limits (section 3.1) would be also useful for avoiding potential violations of the PF1 coil limit. Note that the coil current limits shown in the figures are applied for both positive and negative signs, as the actual limits are only the absolute values of the coil currents.

3. Achievable range of plasma parameters in ITER hybrid operation

We have studied various operation conditions and the achievable range of plasma parameters in ITER hybrid operation. ITER's hybrid operation capability for avoiding the coil current, field and force limits are examined by applying different current ramp rates, and flat-top plasma currents and densities. Modifications to the ramp-down shape evolution and poloidal field coil pre-magnetization [42] were also attempted to further optimize the evolution of the PF2 and PF6 coil currents within their limits. Various combinations of heating and current drive schemes have been compared to investigate several physics issues, such as the plasma current density profile tailoring, enhancement of the plasma energy confinement, fusion power generation, and poloidal flux consumption. The flat-top plasma density and density profile peaking have been varied to examine its impact on the plasma operation conditions. A parameterized edge pedestal model based on EPED1 [17] was applied to several hybrid operation scenarios to improve the modelling of the pedestal evolution and also to check the feasibility of the previously used assumptions on the pedestal.

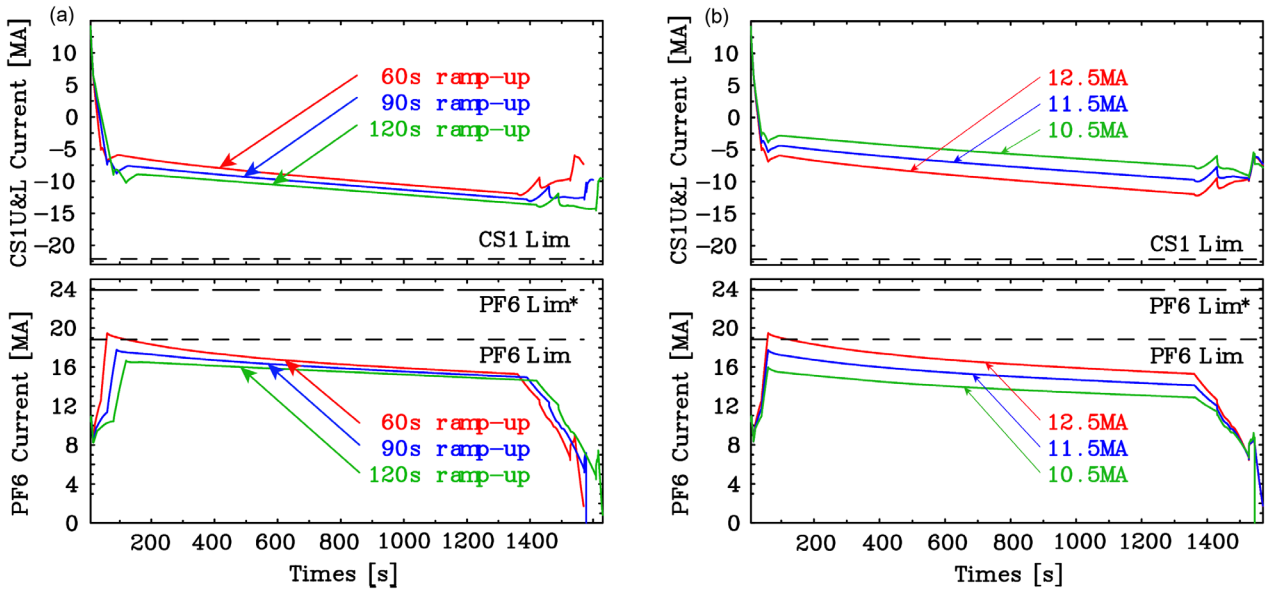

Figure 10. Time traces of CS1 and PF6 coil currents in simulations with various current ramp-up rates (*a*) and at various plasma flat-top currents (*b*). 60 s ramp-up and 12.5 MA cases (shown in red) represent the reference 12.5 MA ITER hybrid operation simulation.

The *L-H* and *H-L* transitions assumed at specified times in the ITER hybrid operation scenarios are also checked by using Martin's *H*-mode threshold power scaling [29], to examine the feasibility of such assumptions.

3.1. Avoiding CS and PF coil current limits

The PF6 coil current, which approaches the coil current limit at the end of the ramp-up phase (see figure 9(*a*)), can be modified to get a higher margin, either by allowing additional consumption of volt-seconds in the PF6 coil or by shifting the initial flux state applied for the tokamak discharge. Applying both techniques seems to be feasible in ITER hybrid operation, whereas those are quite challenging in the 15 MA inductive *H*-mode operation scenario [13, 15]. Ramping up the plasma current to 15 MA and maintaining the current flat-top over a few hundred seconds requires much larger volt-second consumption, therefore demanding the ITER poloidal field coil systems to approach their operation boundaries, leaving little margins of coil currents, forces and fields.

Firstly, allowing additional consumption of the volt-seconds during the current ramp-up is relatively easier than reducing it, as there are several technically feasible methods, such as applying a small bore plasma start-up, delaying the application of auxiliary heating power and reducing the current ramp-up rate. Among these methods, reducing the current ramp-up rate has direct effects on the poloidal field coil systems, rather than on the evolution of the plasma state. Simulations with different current ramp-up rates are compared in figure 10(*a*). The PF6 coil current limit was avoided with reduced current ramp-up rates (90 s or 120 s of current ramp-up) which increase the poloidal flux consumption [43]. However, the volt-second consumption at the CS1 coil has also been increased. This can reduce the duration of the plasma burn if there is not enough margin for the CS1 coil current. As an optimized solution, redistributing the demand on volt-second consumption in the PF6 coil to the other neighbouring coils having enough current margins would be possible by allowing a slight modification of the plasma shape evolution [15]. This optimization has not been yet demonstrated in this work.

Secondly, we have also studied several cases with lower flat-top currents (11.5 MA and 10.5 MA) as shown in figure 10(*b*). In these hybrid operation scenarios, CS and PF coil currents were further from their limits due to the reduced demands on the volt-second consumption during the current ramp-up. These cases show that reducing the flat-top current is favourable in terms of avoiding such coil current limits. However, the plasma temperatures and alpha particle self-heating power were reduced due to the dependence of the plasma confinement on the plasma current. Therefore, the fusion power multiplication factor at a reduced plasma current was smaller ($Q \sim 8.7$ at 11.5 MA, $Q \sim 7.7$ at 10.5 MA) than that achieved in the reference case ($Q \sim 9.6$ at 12.5 MA). As the fusion power multiplication factor is still over 5 and a longer flat-top operation would be possible with more poloidal flux at a reduced flat-top current, a certain range of the flat-top plasma current would be allowable for ITER hybrid operation.

Thirdly, a technique that advances the pre-magnetization of coil systems [42] can be applied to shift the initial flux state, and therefore the CS and PF coil currents. By shifting the initial flux supplied by the coil systems (shown as circles in figure 11(*a*)), the initial current in the PF6 coil (see figure 11(*c*)) can be lowered to avoid the PF6 coil current limit ('PF6 Lim') at around the SOF. However, this technique reduces the available poloidal flux for plasma operation due to the associated shift of CS coil currents closer to its limit (see figure 11(*b*)). Therefore, this method would be useful only when the margin of available poloidal flux is large enough over the operational requirement. Pre-magnetization modelling capability has been added to the CORSICA code, by solving the initial free-boundary equilibrium with a constraint on the flux state. We have studied several cases in which the

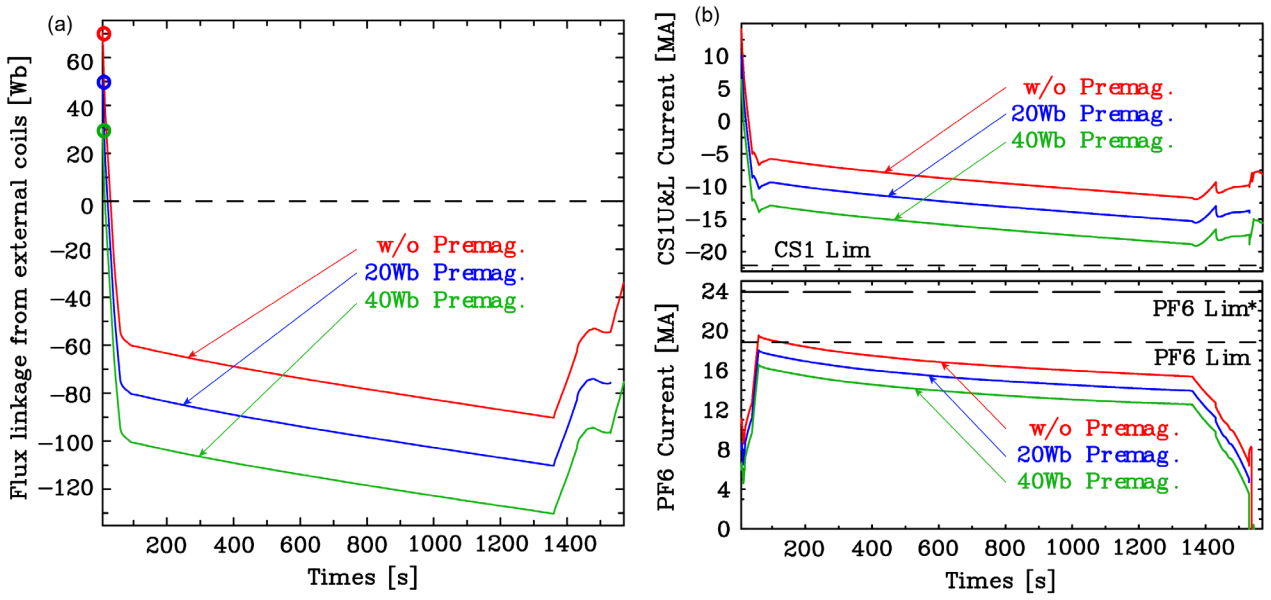

Figure 11. Time traces of the flux linkage from external poloidal field coils (*a*), and CS1 and PF6 coil currents (*b*) in simulations with/without advancing the pre-magnetization. Initial flux states are indicated using circles. The case without advancing the pre-magnetization represents the reference 12.5 MA ITER hybrid operation simulation.

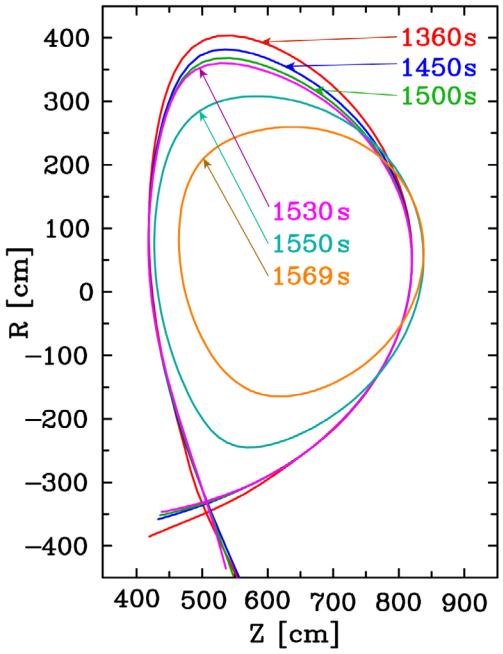

Figure 12. Radially outward plasma shape evolution during the ramp-down. This is modified from the ramp-down shape evolution in the reference 12.5 MA ITER hybrid operation simulation (shown in figure 3(*b*)).

initial flux state is reduced by either 20 Wb or 40 Wb from the value used in the reference simulation, and these are compared in figure 11. The PF6 coil current limit was avoided in both cases with reduced initial flux state, while the plasma shape, profiles, and parameters remained similar to those shown in the reference simulation. The evolution of the flux state was simply shifted as shown in figure 11(*a*), without consuming additional poloidal flux.

The violations of the PF2 coil current, force and field limits shown in figure 9(*b*) have also been investigated. These violations occurred when the plasma was moving downward and the internal inductance significantly increased during the ramp-down phase. With such violations on the ITER plasma control system [44], the plasma can experience an uncontrolled vertical displacement event leading to a disruptive plasma evolution. However, the plasma was in *L*-mode with no auxiliary heating power and the plasma current was about 3.5 MA. This plasma might be allowed to experience a disruptive behaviour without exceeding limits for forces and heat loads. Nevertheless, this situation is unfavourable. Therefore, another simulation assuming a different ramp-down shape evolution (see figure 12) has been attempted to see if this can be avoided. The plasma was moved radially outward while the shape transition from a diverted to limited configuration was allowed to happen at similar time ($t \sim 1550$ s). The evolution of PF2 and PF5 coil currents and fields is shown in figure 13(*b*), for a comparison with those from the reference scenario shown in figure 9(*b*). The evolution of the PF2 coil current and field were well within the limits, and the evolution of the PF1 and PF6 coil currents and fields were significantly stabilized. However, this example does not imply that the downward plasma shape evolution should be avoided. A closer look on the violations in the reference scenario revealed that those had happened mainly due to the rapid shape transition from a diverted to a limited configuration at around $t = 1550$ s, rather than the downward movement during the ramp-down phase (see figure 3(*b*)). A further optimization of the shape transition would give some alternative solutions which allow the plasma to move downward during the ramp-down. As there are still many uncertainties in optimizing the ramp-down shape evolution for ITER, it will be very important to conduct dedicated current ramp-down and termination studies taking the thermal

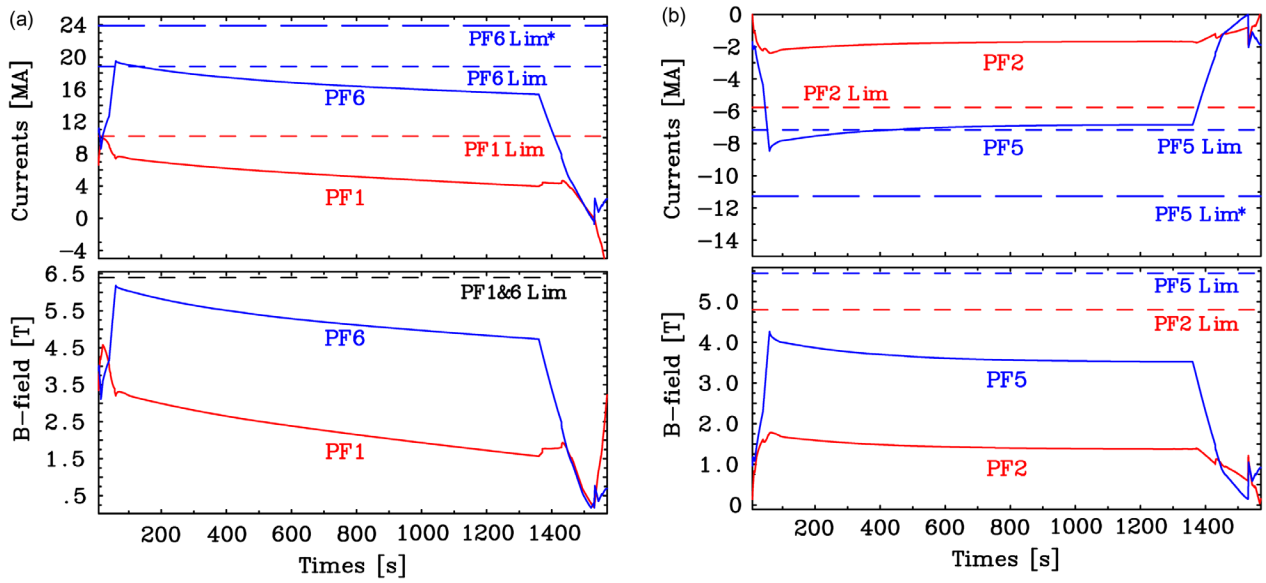

Figure 13. Time traces of the PF1&6 coil currents and applied *B*-field (*a*), and PF2&5 coil currents and *B*-fields (*b*) in the simulation with the modified ramp-down shape evolution (shown in figure 12).

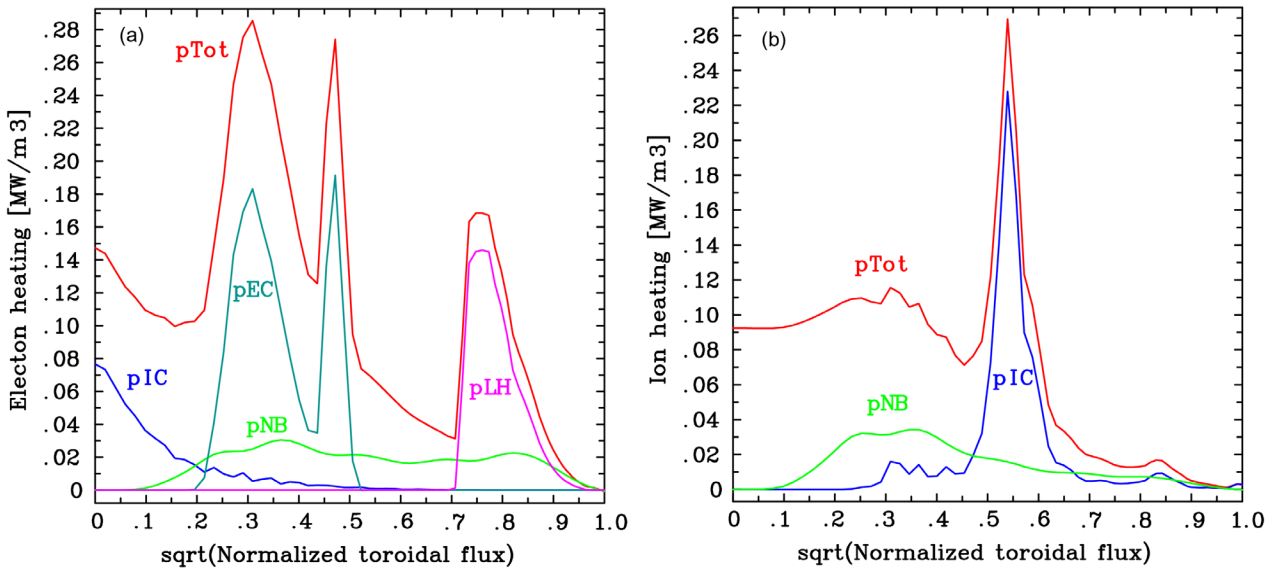

Figure 14. Auxiliary and total heating power deposition profiles to electrons (*a*) and ions (*b*) at $t = 60$ s. 33 MW NB, 20 MW EC, 20 MW LH and 20 MW IC are applied (NB33/EC20/LH20/IC20 case).

heat load constraints on the plasma facing components into account.

3.2. Application of various combinations of H&CD systems

Application of auxiliary H&CD plays a critical role in achieving improved confinement in the hybrid operating mode. Triggering *L-H* and *H-L* transitions, tailoring the plasma current density and safety factor profiles, and controlling the alpha particle self-heating power significantly rely on possible combinations of auxiliary H&CD systems and their operational capabilities. Several simulations have been done to investigate various H&CD schemes considered to be available and their effects on ITER hybrid operation. Four different levels of auxiliary H&CD power, 53 MW for the reference H&CD scheme (33 MW NB & 20 MW EC), 73 MW, 93 MW and 60 MW (without NB) were applied and compared. In the three simulations with 73 MW of auxiliary power, 20 MW of power is added to the reference H&CD scheme (53 MW) using either EC, IC or LH as an additional auxiliary H&CD system. In the 93 MW case, both 20 MW of LH and 20 MW of IC were added to the reference H&CD scheme. Lastly in the two 60 MW cases, 40 MW of EC was applied with either 20 MW of IC or 20 MW of LH, without applying the NB H&CD. The main plasma parameters from these simulations are summarized in table 1.

Second harmonic tritium IC heating at a frequency of 46 MHz was used to provide on-axis electron and off-axis ion heat deposition. Note that fundamental frequency ^{3}He minority ion heating would be also possible [45] for more efficient second

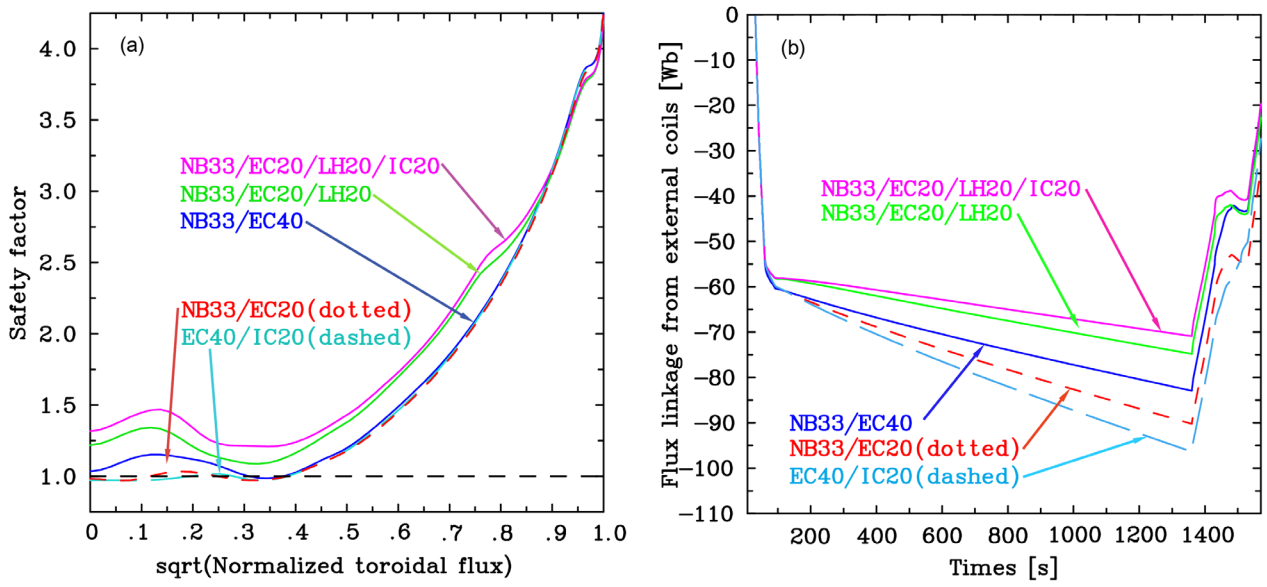

Figure 15. Safety factor profiles at $t = 1359$ s (*a*) and time traces of the flux states (*b*) are compared with simulations with various combinations of H&CD systems.

harmonic tritium IC heating in the presence of fast ions. About 1/3 of the IC power was deposited to the electrons and the rest to the ions, and the IC driven current was not taken into account due to the modelling uncertainties and numerical difficulties in computation. The electron and ion power deposition profile shapes were chosen to be similar to those calculated with the off-line full IC wave propagation/deposition modelling result using the TORIC code [46] (see figure 14), and re-normalized to deliver the total IC power assumed. Additional simulations have been performed to check whether the choice of off-axis ion heating has any significant impact on the hybrid operation scenarios. However, the changes in the scenarios were not significant, even when both on-axis electron and ion heat deposition profiles were assumed with an IC wave frequency of 53 MHz. Note that the use of the fast wave driven current which would have an impact on the evolution of the safety factor at the plasma core is not yet fully considered in this work. LH heat deposition and driven current profiles at a frequency of 5 GHz were computed using a ray-tracing code, LSC [47], assuming only 1 launcher with $n_{||} = 2.2$ for simplicity. The LH wave deposited its power to the electrons around $\rho_{\mathrm{tor}} = 0.7$–$0.9$ (see figure 14). The LH driven current was about 0.9 MA for 20 MW of heating power as shown in table 1. The LHCD efficiency (η) estimated using the formula given in [48] was about $0.22 \times 10^{20}\,\mathrm{Am^{-2}\,W^{-1}}$, similar to the values reported in several publications [11, 48–50]. This LHCD efficiency has been obtained with 100% forward wave directivity assumed for simplicity in this work, while more realistic estimations were done using 2D Fokker Planck models at a reduced forward directivity of 70–87% [48, 49]. A further quantitative study with more realistic LHCD modelling assumptions would be useful to evaluating the effectiveness of off-axis current drive for hybrid operation.

Comparison of the simulation results (see figure 15) has provided some information useful for optimizing ITER hybrid operation scenarios. Firstly, when a far off-axis driven current, such as LHCD, was applied, the internal inductance was effectively reduced (see table 1) and the safety factor profile was maintained over 1.0 until the EOF (figure 15(*a*)). The far off-axis LH driven current ($\rho_{\mathrm{tor}} \sim 0.8$) was effective in increasing the safety factor values inside the driven current deposition location (compare NB33/EC20/LH20 and NB33/EC40 cases). Secondly, the poloidal flux consumption during the flat-top phase was significantly reduced (figure 15(*b*)) with larger non-inductively driven currents. Application of 20 MW of additional LHCD was more effective than 20 MW of additional ECCD, as the LHCD efficiency was higher (compare NB33/EC40 and NB33/EC20/LH20 cases). The effect of pure heating on the poloidal flux consumption (compare NB33/EC20/LH20 and NB33/EC20/LH20/IC20) has been also observed when there was 20 MW of additional IC heating power (no IC driven current assumed). Thirdly, the bootstrap current and alpha particle self-heating power increased along with the auxiliary heating power. However, the fusion power multiplication factor was reduced as the global energy confinement was degraded with additional auxiliary heating power (see table 1). Lastly, in the cases with 60 MW auxiliary power (EC40/LH20 and EC40/IC20, without NB), the achieved plasma parameters were similar to those obtained in the reference simulation (53 MW), except for the poloidal flux consumption and internal inductance, which are dependent on the application of non-inductively driven current. Note that the effects of the early H&CD application during the ramp-up phase on tailoring the plasma current density profile and saving poloidal flux consumption [16] were not yet extensively investigated in this work and further optimization is possible.

3.3. Varying the flat-top plasma density and density profile peaking

The flat-top plasma density and density profile peaking have been varied to examine their influences on the plasma

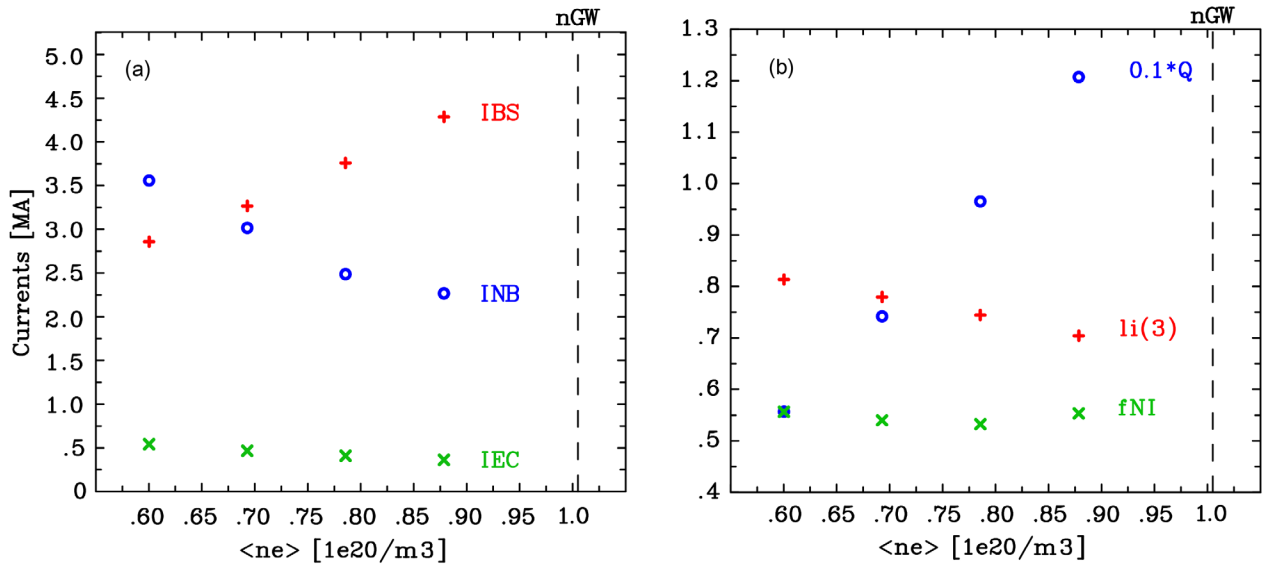

Figure 16. The bootstrap current, NB and EC driven currents (*a*), non-inductively driven current fraction, internal inductance and fusion power multiplication factor multiplied by 0.1 (*b*) at various flat-top electron densities. The Greenwald density limit is shown with vertical dotted lines.

performance and operation conditions. The main plasma parameter dependency on the flat-top plasma density has been shown in figure 16. The Greenwald density limit, an indicator for the allowed plasma operation space, is shown with vertical dashed lines.

As the volume averaged flat-top plasma density ($\langle n_e \rangle$) is increased from $6.0 \times 10^{19}\,\mathrm{m}^{-3}$ to $8.8 \times 10^{19}\,\mathrm{m}^{-3}$, the NB driven current is quickly reduced. The EC driven current was weakly dependent on the flat-top plasma density, whereas the bootstrap driven current, which is strongly dependent on the pressure gradient, was increased along with the flat-top density. Therefore, the total non-inductively driven current fraction, f_{NI}, remains at a quite similar level for a wide range of the flat-top density. The internal inductance was reduced along with the flat-top density, due to a broadening of the current density profile from both the increase in the bootstrap current in the pedestal region and the decrease of the NB driven current in the core region. A very strong variation was observed in the fusion power multiplication factor (Q). It increased from 5.6 at $\langle n_e \rangle = 6.0 \times 10^{19}\,\mathrm{m}^{-3}$ to 12.1 at $\langle n_e \rangle = 8.8 \times 10^{19}\,\mathrm{m}^{-3}$, due to a strong increase in alpha heating power. In these simulations, the plasma temperatures achieved in the core region were quite similar while the flat-top density significantly varied. The plasma confinement enhancement factor (H_{98}) slightly increased from 1.17 to 1.27 along with the flat-top density. The plasma temperatures in the pedestal region were slightly reduced when the flat-top plasma density was increased. However, the pedestal pressure slightly increased as the plasma confinement was not significantly degraded along with the flat-top plasma density. It appears that this pedestal pressure dependence on the pedestal density qualitatively agrees with the EPED1 pedestal prediction [27]. Note that the Coppi–Tang transport model [32] was used to compute the heat diffusivities and to model the *H*-mode pedestal and the parameterized edge pedestal model based on EPED1 was not yet applied for this study.

In this plasma parameter scan study, increasing the flat-top plasma density and maintaining it during the burn is identified as a good candidate for achieving ITER hybrid operation with a high Q value. Another important plasma parameter that would also be quite beneficial for achieving a high Q value is the density peaking factor. Although the achievable range of the density peaking factor [51, 52] is still uncertain and reliable density profile control technique is required to be developed, it would be useful to perform a parameter scan on the density profile peaking factor. Four simulations were performed with different density profile peaking factors (see figure 17). The plasma density at the pedestal was reduced as the core density increased to keep the volume averaged electron density similar ($\sim 7.7 \times 10^{19}\,\mathrm{m}^{-3}$). This has been done to distinguish the effects of varying density peaking factor with those of varying the volume averaged flat-top density. Note that the parameterized edge pedestal model based on EPED1 is used in these simulations to better model the density profile peaking and pedestal parameters. The fusion power multiplication factor, electron temperature at the pedestal top (multiplied by 2), non-inductively driven current fraction (multiplied by 10) and bootstrap current are compared in figure 17(*b*). The electron temperature at the pedestal top was increased along with the density profile peaking factor as the pedestal density is reduced. The total bootstrap current and non-inductively driven current fraction was also slightly increased along with the density profile peaking factor due to the increased pressure gradients. The fusion power multiplication factor has been also increased due to the higher density in the core region. However, the variation of the fusion power multiplication factor was moderate. The reference simulation case with a less peaked parabolic density profile (shown with larger black markers) appears to be conservative in terms of fusion power production. Varying both the flat-top plasma density and density peaking factor would also be very useful basis for developing the baseline 15 MA *H*-mode ITER operation where the target Q value is much higher (~10).

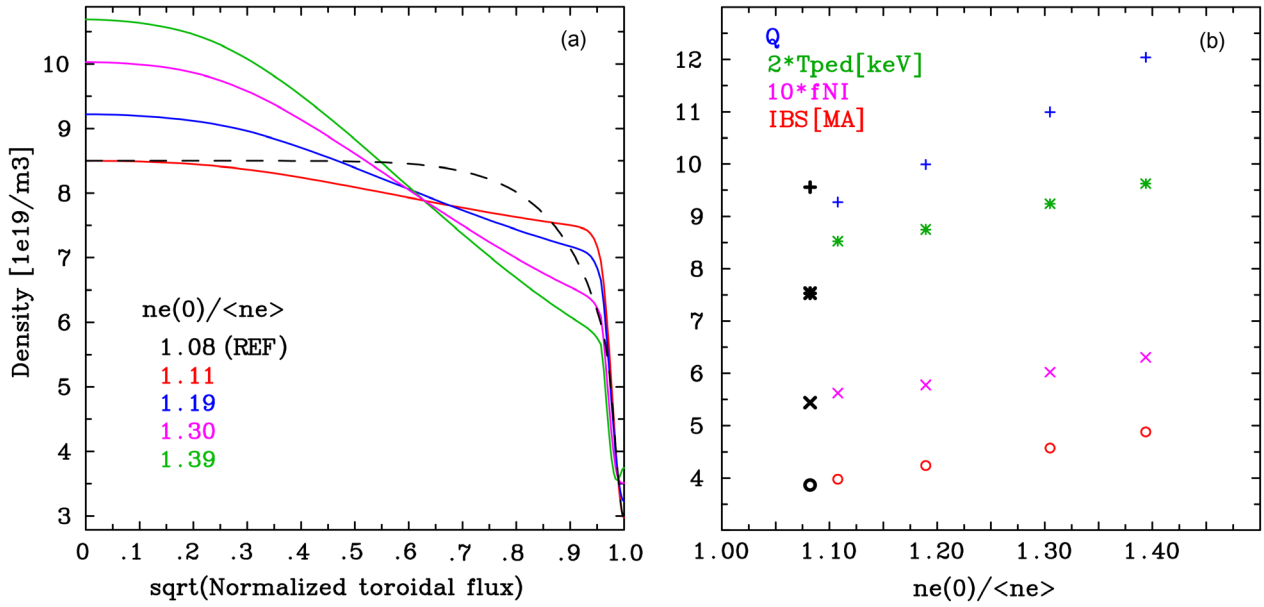

Figure 17. The density profiles with different density profile peaking (*a*), fusion power multiplication factor, electron temperature at the pedestal top (multiplied by 2), non-inductively driven current fraction (multiplied by 10) and bootstrap current (*b*) are compared. The density profiles were prescribed using a hyperbolic pedestal shape and set to have a similar volume averaged electron density (~$7.7 \times 10^{19}\,\mathrm{m}^{-3}$). The reference 12.5 MA ITER hybrid operation simulation with a parabolic density profile (shown with a dashed line in (*a*) and larger black markers in (*b*)) has a slightly higher volume averaged electron density (~$7.9 \times 10^{19}\,\mathrm{m}^{-3}$).

Varying the plasma density evolution during the current ramp-up phase would be an interesting subject to study, as it can modify the *L-H* confinement mode transition and plasma profiles desired at the SOF for hybrid operation. A preliminary comparison using a few test cases has shown that the amount of EC driven current, which is inversely proportional to the electron density, can modify the safety factor profile. Therefore, optimizing the EC current deposition together with the density waveform during the current ramp-up could be a useful tool for tailoring the current density profile desired at the SOF [9]. Note that potential violations of various coil limits associated with varying the plasma density are weak constraints in ITER hybrid operation scenarios and avoidable using the techniques exploited in section 3.2. However, it should be more carefully assessed for the baseline 15 MA *H*-mode ITER operation, which has much less margin for the poloidal field coil systems.

3.4. Plasma edge pedestal modelling

A parameterized edge pedestal model based on EPED1 [27] is coupled to the CORSICA code for a better estimate of the pedestal width and height. This edge pedestal model has 9 input parameters, the total plasma current, electron density at the pedestal, effective charge number, normalized plasma beta, major radius, minor radius, plasma elongation, plasma triangularity and toroidal magnetic field, and 4 output values, pedestal widths and critical pressures at the pedestal (ψ_{ped}) or pedestal top ($\psi_{\mathrm{top}} = 1 - (3/2) \times (1 - \psi_{\mathrm{ped}})$) [53]. To use the edge pedestal model consistent with the original EPED1 description [53] for a time-dependent scenario simulation, the electron density profile shape has been slightly modified. A hyperbolic tangent function used to describe the pedestal density profile is connected to a parabolic function used to describe the core density profile. The resulting electron density profile is given by

$$n_{\mathrm{e}}(\psi) = n_{\mathrm{e0}} \left\{ (1 - r_2) \left(c_1 \left[H\left(1 - \frac{\psi}{\psi_{\mathrm{ped}}}\right)\left(1 - \left(\frac{\psi}{\psi_{\mathrm{ped}}}\right)^{\alpha}\right)^{\beta} \right] + c_2 \left[\tanh\left(2\frac{1-\psi_{\mathrm{mid}}}{1-\psi_{\mathrm{ped}}}\right) - \tanh\left(2\frac{\psi-\psi_{\mathrm{mid}}}{1-\psi_{\mathrm{ped}}}\right) \right] \right) + r_2 \right\},$$

where ψ, n_{e0}, $n_{\mathrm{e}}(\psi_{\mathrm{ped}}) = r_1 n_{\mathrm{e0}}$ and $n_{\mathrm{e}}(\psi = 1) = r_2 n_{\mathrm{e0}}$ are the normalized poloidal flux, electron densities at the plasma centre, pedestal and plasma boundary. The location in the middle between the pedestal and separatrix is given as $\psi_{\mathrm{mid}} = 1 - (1/2) \times (1 - \psi_{\mathrm{ped}})$, and H is the Heaviside step function. The core density profile with a parabolic profile shape is defined using two more parameters, α and β. The two coefficients that connect the core and edge density shape functions across the pedestal location are given as $c_1 \cong 1 - c_2(1 + \tanh(1))$ and $c_2 = (r_1 - r_2)/\{2\tanh(1)(1 - r_2)\}$. The electron density ratios with respect to the central electron density, r_1 and r_2, are used to determine the electron densities at the pedestal and plasma boundary, respectively. In this work, the pedestal and boundary electron densities are respectively assumed to be 80% and 35% of the central electron density ($r_1 = 0.80$ and $r_2 = 0.35$). The core density profile in *H*-mode is assumed to be monotonic using $\alpha = \beta = 1.0$. Note that the pedestal electron density is given as an input and assumed to be independent of the pedestal width and pressure estimated by the edge pedestal model. If the pedestal electron density is allowed to be determined using an iterative re-estimation at the computed pedestal width, it can numerically oscillate or diverge to an unphysical value.

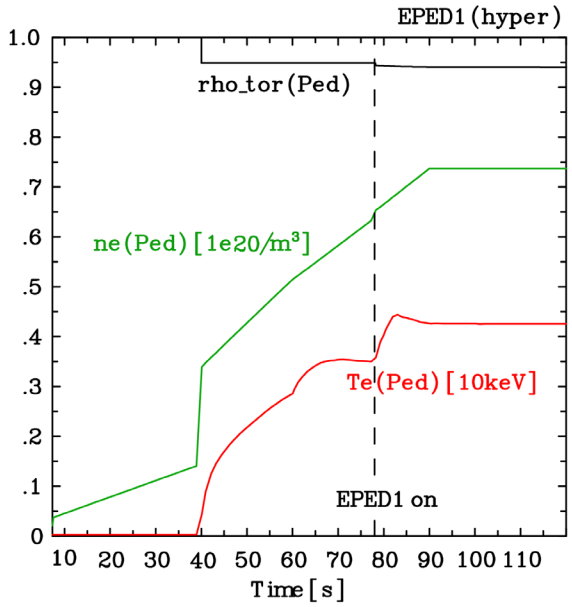

Figure 18. Time traces of the pedestal top location, electron density and temperature. The parameterized edge pedestal model based on EPED1 is switched on at around $t = 78$ s (indicated as a vertical dotted line).

When the parameterized edge pedestal model was applied, the output values (pedestal width and pressure) have been obtained by performing either linear interpolation or extrapolation to cover a wider range of input parameter space. The input parameter ranges for the extrapolation were assumed to be extended up to an additional 50% of the input parameter ranges available for interpolation $\left([x^{\mathrm{ext}}_{\mathrm{left}}, x^{\mathrm{ext}}_{\mathrm{right}}] = \left[x^{\mathrm{int}}_{\mathrm{left}} - 0.5 \times \left|x^{\mathrm{int}}_{\mathrm{left}} - x^{\mathrm{int}}_{\mathrm{right}}\right|, x^{\mathrm{int}}_{\mathrm{right}} + 0.5 \times \left|x^{\mathrm{int}}_{\mathrm{left}} - x^{\mathrm{int}}_{\mathrm{right}}\right|\right]\right)$. Then, the electron and ion heat diffusivities at the edge pedestal were feedback controlled to reproduce the pedestal pressure estimated by the parameterized edge pedestal model. The proportional and derivative gains used for the feedback control were manually adjusted to avoid potential oscillatory behaviours. The estimation of the pedestal parameters using the edge pedestal model became active only when the plasma was within the extended input parameter space. When the plasma was outside the range of input parameter extrapolation, the pre-programmed assumptions for the *H*-mode edge pedestal evolution were applied similarly to the reference hybrid operation scenario.

Figure 18 shows a ITER hybrid operation simulation where the parameterized edge pedestal model is applied. The edge pedestal formation started at about $t = 40$ s, following the *L-H* confinement mode transition specified. The parameterized edge pedestal model became active at around $t = 78$ s, as the plasma parameters became available for the extrapolation. When the parameterized edge pedestal model started, the pedestal electron density evolution had almost no perturbation as the pedestal density was used as an input. The evolution of the pedestal width ($\Delta\rho_{\mathrm{tor}} \sim 0.05$) has also shown a small perturbation as the value estimated by the parameterized edge pedestal model was slightly larger. However, the pedestal electron temperature has been increased over 4 keV by reducing the heat diffusivities at the pedestal region.

The time-traces of the pedestal parameters in this simulation are compared with those in the reference hybrid simulation (section 2) in which a parabolic pedestal density shape is prescribed with a pre-programed reduction of the heat diffusivities for edge pedestal evolution. The dynamic evolution of the pedestal parameters is shown in figure 19(*a*) and the pedestal electron density and temperature profiles at $t = 200$ s are compared in figure 19(*b*). When the parameterized edge pedestal model was applied, the feedback controlled pedestal top pressure and width were respectively higher and larger than those assumed in the reference simulation. This implies that the previously conducted ITER hybrid operation simulations underestimated the stability-based limits for these parameters and therefore plasma performance appears to be slightly reduced. Note that the total bootstrap current was not so different with the value obtained in the reference simulation, as the reduction in the bootstrap current at the pedestal region has been compensated by the increase of it at the core region. As the same central plasma density is assumed, the increase of density gradients in the pedestal region inevitably reduces density gradients in the core region, and vice versa in the reference simulation. Application of the parameterized edge pedestal model based on EPED1 has been implemented and tested in this work, aiming at applying it routinely to diverse simulations. Note that the extension of the EPED1 data set for interpolation and extrapolation to a wider range of operational space will be a subject of future development.

3.5. *L-H transition modelling during the ramp-up*

In the reference simulation and also in the other variants, the *L-H* transition has been assumed to be triggered at a specified time for simplicity, without introducing a detailed evaluation of the *H*-mode threshold power as a triggering condition. This simple assumption is based on the general idea that the auxiliary heating power available for ITER hybrid operation is enough to trigger an *L-H* transition in DT plasmas at a desired time in between the ramp-up and flat-top phases, unless the other constraints on the auxiliary heating systems, such as the NB power shine-through limit, become an issue. In addition, a little variance in the timing of the *L-H* transition would not make significant modifications to the overall plasma performance, if the necessary conditions for hybrid operation can be achieved at the SOF. Note also that there are still a non-negligible amount of uncertainties in the *H*-mode threshold power scaling laws considered for ITER projection.

To investigate the feasibility of the assumption used for triggering the *L-H* confinement mode transition in the reference simulation ($tL2H = 40$ s), we have compared it with the Martin's *H*-mode threshold power scaling law [29] developed for ITER projection. The evolution of the loss power estimated during the current ramp-up and at the beginning of the flat-top phase is shown in figure 20. The *H*-mode threshold power computed using the Martin scaling law is also shown as a dashed line. It appears that an *L-H* transition is likely to happen around $t = 60$ s in the reference simulation (in red dotted line) if the Martin scaling is applied, differently with the assumption used in the simulation. To compare this

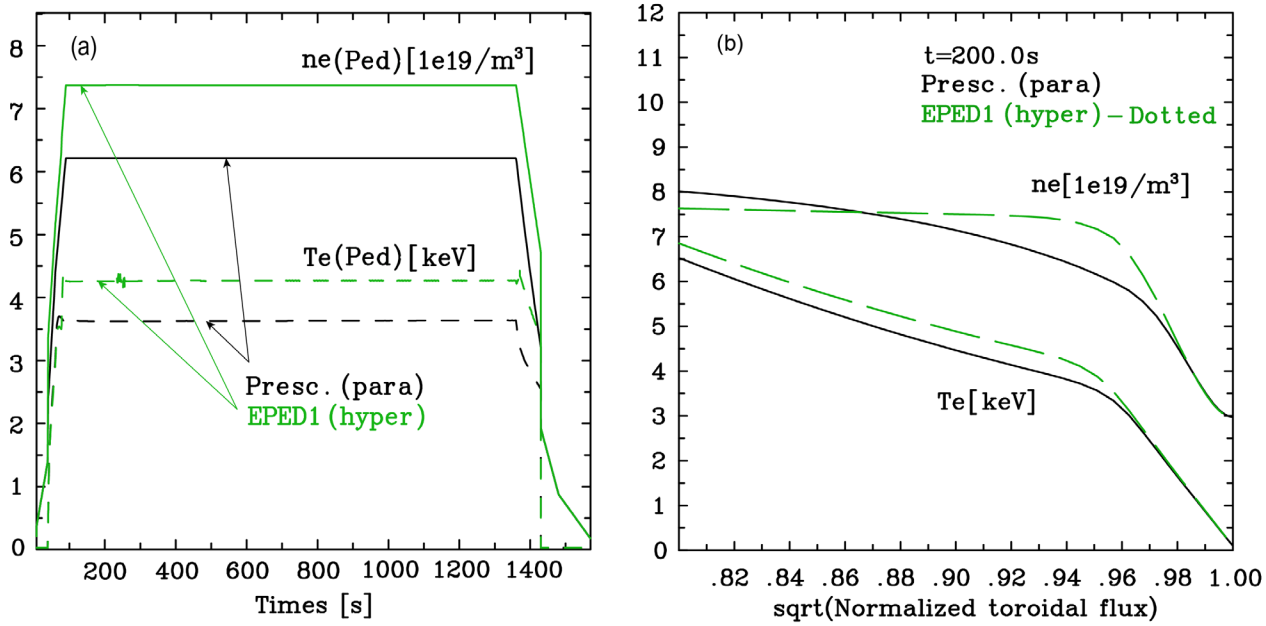

Figure 19. Time traces of the electron density and temperature at the pedestal top (*a*) and density and temperature profiles (*b*) at the edge region. The reference simulation with a parabolic electron density profile shape is indicated as 'Presc. (para)'. The simulation using the parameterized edge pedestal model with a hyperbolic pedestal density profile shape is indicated as 'EPED1 (hyper)'. The pedestal pressure estimated using the parameterized edge pedestal model is higher than that assumed in the reference simulation.

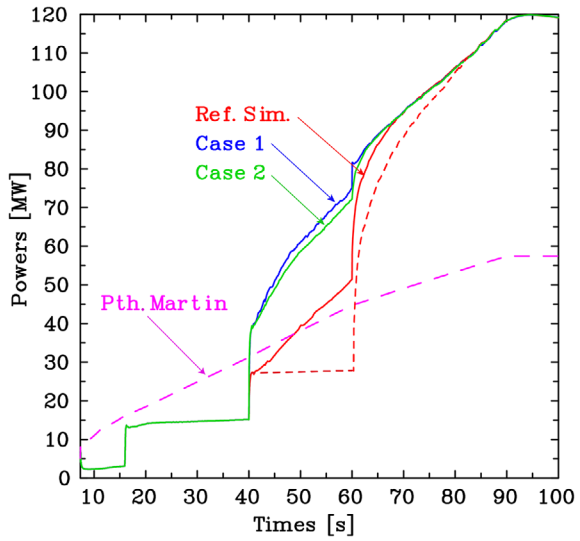

Figure 20. Time traces of the estimated loss power and the power estimated using Martin's *H*-mode threshold power scaling law (dashed line). The cases with an early application of additional auxiliary heating power are indicated as Case 1 and Case 2. If the Martin scaling law is applied to the reference simulation, an *L*-*H* confinement mode transition will be triggered at around $t = 60$ s (the time trace of the loss power is likely to follow the red dotted line).

simulation with other simulations in which an *L*-*H* transition is likely to happen at $t = 40$ s in accordance with the assumption made, 2 simulations have been performed with earlier application of additional auxiliary heating power. In case 1, the second NB source (16.5 MW) is switched on at $t = 40$ s. In case 2, it is assumed that 8.25 MW of NB power (half of the second NB source power) is switched on with 6.77 MW of additional EC power at $t = 40$ s. In both cases, the second NB source power is increased to its full power (16.5 MW) at $t = 60$ s. In these cases with early application of additional heating power, the estimated loss power became higher than the Martin *H*-mode threshold power at $t = 40$ s, implying that the earlier triggering an *L*-*H* transition is feasible for ITER hybrid operation. Comparison of achieved plasma parameters between these two cases and the reference simulation shows that the evolution of the plasma safety factor and poloidal flux consumption during the ramp-up has been slightly modified. However, no significant modification of the overall plasma performance during flat-top operation has been observed.

4. Full free-boundary control simulation

Self-consistent free-boundary transport simulations have been performed to provide information on the CS/PF coil voltage demands and to study the controllability with the ITER controllers, JCT2001 and VS1 (see figure 1). Note that the choice of ITER controllers will be finalized later as controllers are to be further developed and tested along with the development of the ITER plasma control system (PCS) [44]. In these simulations, the coil currents obtained from the prescribed boundary transport simulations were used to set the reference coil currents for the controllers, shown as dotted lines in figure 21. Each reference coil current consists of a series of straight lines, as only a few time-slices were chosen to set the reference current waveform for simplicity. The CS/PF coil currents were well feedback controlled around the reference coil currents. Note that this free-boundary transport simulation has been done with the modified ramp-down shape evolution (see figure 12). The major differences between the reference coil currents and feedback controlled coil currents were observed

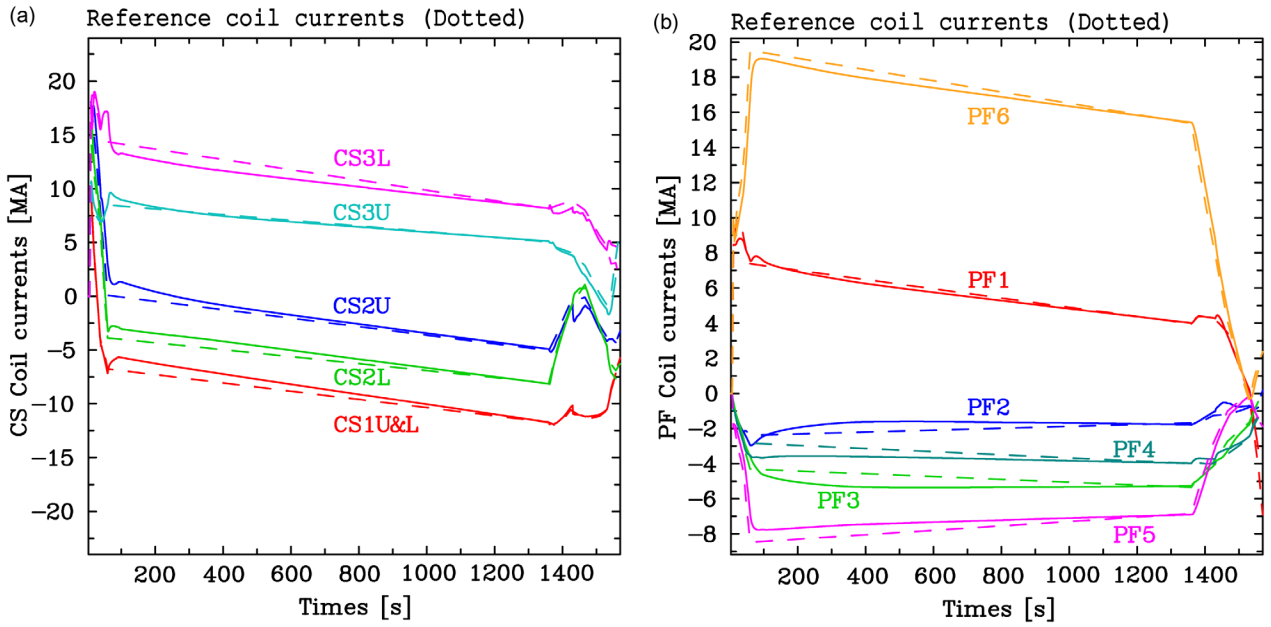

Figure 21. Time traces of the CS (*a*) and PF (*b*) coil currents in the full free-boundary simulation. Dotted lines represent the reference coil current waveforms used for controllers, which are obtained in the simulation with modified ramp-down shape (shown in figure 12).

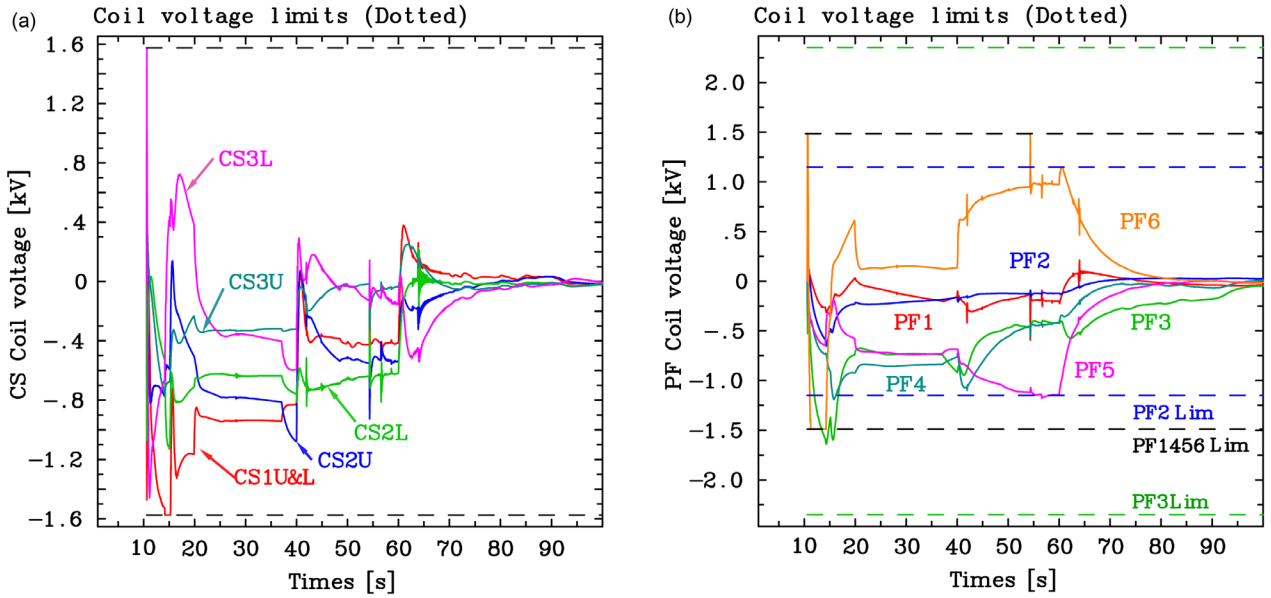

Figure 22. Time traces of the CS (*a*) and PF (*b*) coil voltage during the current ramp-up and at the beginning of the flat-top phases in the full free-boundary simulation (tDIV ~ 15 s, $tL2H$ ~ 40 s and tSOF ~ 60 s). Dotted lines represent coil voltage limits.

around the start of flat-top phase (see figure 21), as the reference coil current waveforms did not reflect the detailed plasma evolution after the *L-H* confinement mode transition, where the bootstrap current was quickly increased. If more time-slices around the *L-H* transition are added in specifying the reference coil current waveforms, the observed differences will be reduced in the free-boundary simulations. The evolution of plasma parameters and profiles were very similar to those obtained from the prescribed boundary transport simulations.

The evolution of voltages applied on the CS and PF coils during the current ramp-up and at the beginning of the flat-top phase is shown in figure 22. The power supply voltage demands were well within their limits, as the coil voltage limits were used as saturation voltages for the power supply models. The voltage demand on the VS1 coil system was also well within its limit as the plasma was not subjected to a strong vertical instability. However, several large voltage fluctuations are observed when the plasma experiences a shape transition from a limiter to a diverter configuration and vice versa, *L-H* and *H-L* confinement mode transitions, and following application of auxiliary heating powers. As the plasma becomes stationary at the beginning of the flat-top phase, coil voltage demands become much smaller compared to their limits.

The evolution of 6 gap signals measured at the gap locations for shape control (see figure 1) is shown in figure 23.

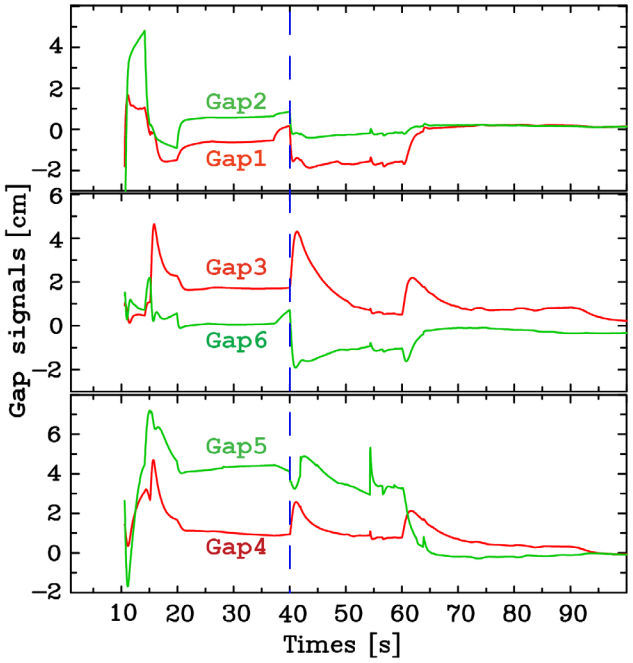

Figure 23. Time traces of the gap measurement signals ($\sim\delta\psi/|\nabla\psi|$) in the full free-boundary simulation (tDIV ~ 15 s, t*L*2*H* ~ 40 s and tSOF ~ 60 s). The gap measurement locations used for the plasma shape control are shown in figure 1.

These gap signals ($\sim\delta\psi/|\nabla\psi|$) were obtained by measuring the difference of the poloidal flux with the reference value computed for given boundary shape ($\delta\psi$) and then dividing it by the poloidal flux gradient at the plasma boundary ($|\nabla\psi|$). Therefore the gap measurement signal does not indicate the real distance between the plasma boundary and plasma facing components, but shows an approximate deviation of the poloidal flux from the reference value at the measurement location. These are useful measurement signals for plasma boundary flux control as one of the shape control methods. Large fluctuations in the gap measures were observed when there were fluctuations in the CS and PF coil voltages. During the *L*-*H* transition at around $t = 40$ s, the plasma boundary moved outward as shown in the gap signals of Gap3 (poloidal flux increased) and Gap6 (poloidal flux decreased). When the auxiliary heating power was increased at around $t = 60$ s, similar changes were observed.

The plasma vertical stability dynamics has been also studied by repeating this simulation with a triggered vertical displacement event (VDE). The feedback control loops were disconnected at about $t = 350$ s, and then the plasma moved up with a triggered vertical displacement event as shown in figure 24. The vertical instability growth rate computed using the logarithmic estimation method [15] was about 3–4 s^{-1} (see the nested figure in figure 24). This value is smaller than that obtained from the 15 MA *H*-mode scenarios [54], implying that the vertical stabilization of the plasma position in ITER hybrid operation will be feasible with enough control margin. However, as the control margin for the vertical instability is known to be reduced for the plasma with a high internal inductance and low plasma beta [54], a further study will be required for the current ramp-up and ramp-down phases.

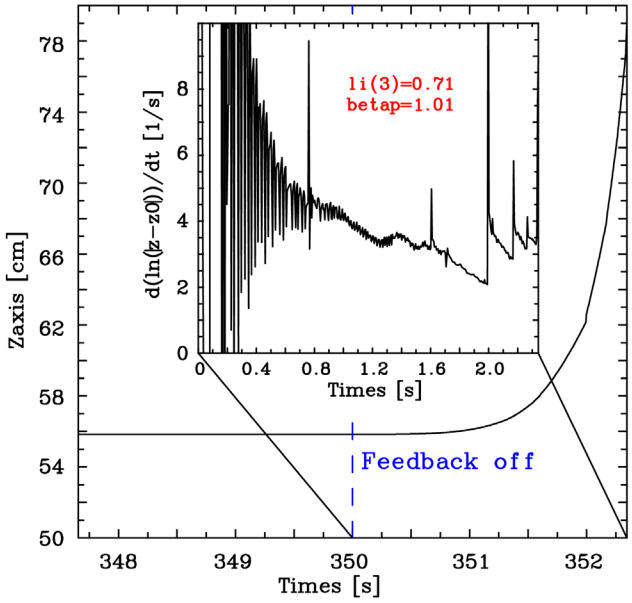

Figure 24. Time traces of the vertical plasma position and estimated vertical instability growth rate (in the nested figure). The feedback control loops are disconnected at about $t = 350$ s to trigger a vertical displacement event.

5. Summary and discussion

ITER hybrid operation scenarios have been studied using an advanced free-boundary transport simulation code, CORSICA, including relevant physics, engineering constraints, and ITER design parameters. Accessible ITER hybrid operation conditions and achievable range of plasma parameters have been investigated considering uncertainties on the plasma confinement and transport. Useful techniques for avoiding the poloidal field coil current, field and force limits, such as applying different current ramp rates, flat-top plasma currents and densities, and pre-magnetization of the poloidal field coils have been tested and ITER operation capability with such techniques has been assessed. Several tokamak physics issues, such as plasma current density profile tailoring, enhancement of the plasma energy confinement, and fusion power generation have been studied with various combinations of H&CD schemes foreseen for ITER advanced operation. An edge pedestal model based on EPED1 parameterization has been applied to check the assumptions previously used and to improve scenario modelling. Fully self-consistent free-boundary transport simulations have been performed to provide information on the poloidal field coil voltage demands and to study the controllability with the ITER controllers.

The studies conducted in this work show that operating ITER in the hybrid operating mode is feasible and there are many useful techniques to be applied and further developed. Optimization of the operation scenarios will be continued as the requirements for ITER systems and understanding on the tokamak physics will be further elaborated. The studies done in this paper will be a useful basis for further studies, such as active burn control, plasma termination with disruption avoidance, density peaking and its control, advanced H&CD

control schemes, and actuator sharing. These studies will contribute to developing ITER steady-state operation scenarios and exploiting long-pulse ITER operations. Performing integrated magnetic and kinetic control simulations [55] would be also an important development of this modelling platform, which is open for adapting many different physics and control components. The improved tokamak discharge modelling capability achieved in this work will be useful for supporting the ITER PCS [44], and Integrated Modelling (IM) development [26].

Acknowledgments

The authors wish to thank Drs C.E. Kessel and J. Garcia for fruitful discussions, Dr P.B. Snyder for providing EPED1 results, and Drs M. Henderson and T. Oikawa for providing ITER EC and NB design parameters. This work was partly supported by the Principality of Monaco/ITER Postdoctoral Research Fellowship Program. The views and opinions expressed herein do not necessarily reflect those of the ITER Organization.

References

[1] Luce T.C. *et al* 2003 *Nucl. Fusion* **43** 321
[2] Staebler A. *et al* 2005 *Nucl. Fusion* **45** 617
[3] Joffrin E. *et al* 2005 *Nucl. Fusion* **45** 626
[4] Horbirk J. *et al* 2012 *Plasma Phys. Control. Fusion* **54** 095001
[5] Turco F. *et al* 2015 *Phys. Plasmas* **22** 056113
[6] Casper T.A. *et al* 2007 *Nucl. Fusion* **47** 825
[7] Jardin S.C. *et al* 2015 *Phys. Rev. Lett.* **115** 215001
[8] Hogeweij G.M.D. *et al* 2013 *Nucl. Fusion* **53** 013008
[9] Besseghir K. *et al* 2013 *Plasma Phys. Control. Fusion* **55** 125012
[10] Citrin J. *et al* 2010 *Nucl. Fusion* **50** 115007
[11] Kessel C.E. *et al* 2007 *Nucl. Fusion* **47** 1274
[12] Giruzzi G. *et al* 2011 *Plasma Phys. Control. Fusion* **53** 124010
[13] Casper T.A. *et al* 2014 *Nucl. Fusion* **54** 013005
[14] Crotinger J.A. *et al* 1997 *LLNL Report* UCRL-ID-126284; NTIS #PB2005-102154
[15] Kim S.H. *et al* 2009 *Plasma Phys. Control. Fusion* **51** 105007
[16] Kim S.H. *et al* 2009 *Plasma Phys. Control. Fusion* **51** 065020
[17] Poli F.M. *et al* 2014 *Nucl. Fusion* **54** 073007
[18] Poli F.M. *et al* 2013 *Phys. Plasmas* **20** 056105
[19] Budny R.V. *et al* 2008 *Nucl. Fusion* **48** 075005
[20] Koechl F. *et al* 2012 *Proc. 39th EPS Conf. on Plasma Physics (Stockholm, 2012)* vol 36 P-1.042 http://ocs.ciemat.es/epsicpp2012pap/pdf/P1.042.pdf
[21] Parail V. 2013 *Nucl. Fusion* **53** 113002
[22] Kalupin D. *et al* 2013 *Nucl. Fusion* **53** 123007
[23] Falchetto G.L. *et al* 2014 *Nucl. Fusion* **54** 043018
[24] Jardin S.C. *et al* 1986 *J. Comput. Phys.* **66** 481
[25] Kepler Project https://kepler-project.org
[26] Imbeaux F. *et al* 2015 *Nucl. Fusion* **55** 123006
[27] Snyder P.B. *et al* 2011 *Nucl. Fusion* **51** 103016
[28] Casper T.A. *et al* 2008 *Fusion Eng. Des.* **83** 552–6
[29] Martin Y.R. *et al* 2008 *J. Phys.: Conf. Ser.* **123** 012033
[30] Lukash V.E. *et al* 2005 *Plasma Devices Oper.* **13** 143
[31] Pearlstein L.D. *et al* 2006 *Proc. 33rd EPS Conf. on Plasma Physics (Rome, 2006)* vol 30I P-5.128 http://epsppd.epfl.ch/Roma/pdf/P5_128.pdf
[32] Jardin S.C. *et al* 1993 *Nucl. Fusion* **33** 371
[33] Tang W.M. 1986 *Nucl. Fusion* **26** 1605
[34] Singh M.J. *et al* 2015 *AIP Conf. Proc.* **1655** 050011
[35] Oikawa T. 2011 private communication
[36] Farina D. *et al* 2012 *Nucl. Fusion* **52** 033005
[37] Lin-Liu Y.R. *et al* 1997 *Radio Frequency Power in Plasmas: 12th Topical Conf. (Savannah, 1997)* vol CP403 p 195 https://inis.iaea.org/search/searchsinglerecord.aspx?recordsFor=SingleRecord&RN=29000266
[38] Henderson M. *et al* 2015 *Phys. Plasmas* **22** 021808
[39] Farina D. *et al* 2015 *Phys. Plasmas* **21** 061504
[40] Henderson M.A. *et al* 2012 *Proc. 24th Int. Conf. on Fusion Energy (San Diego, 2012)* (Vienna: IAEA) CD-ROM file (ITR/P1-06) and www-naweb.iaea.org/napc/physics/FEC/FEC2012/fec12.htm
[41] Gribov Y. 2011 ITER D 2ACJT3 private communication
[42] Kessel C.E. *et al* 2010 *Proc. 23rd Int. Conf. on Fusion Energy (Daejeon, 2010)*(Vienna: IAEA) CD-ROM file (ITR/P1-22) and www-naweb.iaea.org/napc/physics/FEC/FEC2010/index.htm
[43] Luce T.C. *et al* 2014 *Nucl. Fusion* **54** 093005
[44] Snipes J.A. *et al* 2010 *Fusion Eng. Des.* **85** 461
[45] Budny R.V. *et al* 2012 *Nucl. Fusion* **52** 023023
[46] Brambilla M. 1999 *Plasma Phys. Control. Fusion* **41** 1
[47] Ignat D.W. *et al* 1994 *Nucl. Fusion* **34** 837
[48] Decker J. *et al* 2011 *Nucl. Fusion* **51** 073025
[49] Bonoli P.T. *et al* 2006 *Proc. 21st Int. Conf. on Fusion Energy (Chengdu, 2006)* (Vienna: IAEA) CD-ROM file (IT/P1-2) and www-naweb.iaea.org/napc/physics/FEC/FEC2006/index.htm
[50] Hoang G.T. *et al* 2009 *Nucl. Fusion* **49** 075011
[51] Angioni C. *et al* 2007 *Nucl. Fusion* **47** 1326
[52] Zohm H. *et al* 2013 *Nucl. Fusion* **53** 073019
[53] Snyder P.B. *et al* 2004 *Plasma Phys. Control. Fusion* **46** A131
[54] Portone A. *et al* 2005 *Fusion Eng. Des.* **74** 537
[55] Kim S.H. *et al* 2012 *Nucl. Fusion* **52** 074002